Brigham Young University
BYU ScholarsArchive

Theses and Dissertations

2019-08-01

Studies of Dislocation Density Quantification Via Cross-Correlation EBSD

Samuel Searle Friedbaum
Brigham Young University

Follow this and additional works at: https://scholarsarchive.byu.edu/etd

BYU ScholarsArchive Citation

Friedbaum, Samuel Searle, "Studies of Dislocation Density Quantification Via Cross-Correlation EBSD" (2019). *Theses and Dissertations*. 8115.
https://scholarsarchive.byu.edu/etd/8115

This Thesis is brought to you for free and open access by BYU ScholarsArchive. It has been accepted for inclusion in Theses and Dissertations by an authorized administrator of BYU ScholarsArchive. For more information, please contact scholarsarchive@byu.edu, ellen_amatangelo@byu.edu.

Studies of Dislocation Density Quantification Via Cross-Correlation EBSD

Samuel Searle Friedbaum

A thesis submitted to the faculty of
Brigham Young University
in partial fulfillment of the requirements for the degree of

Master of Science

David T. Fullwood, Chair
Eric R. Homer
Oliver K. Johnson

Department of Mechanical Engineering

Brigham Young University

Copyright © 2019 Samuel Searle Friedbaum

All Rights Reserved

ABSTRACT

Studies of Dislocation Density Quantification Via Cross-Correlation EBSD

Samuel Searle Friedbaum
Department of Mechanical Engineering, BYU
Master of Science

One conventional method for studying dislocations uses the Transmission Electron Microscope (TEM), a complex and expensive piece of equipment which requires extensive specimen preparation in order to thin the specimens to electron transparent thickness. Newer High Resolution Electron Backscatter Diffraction (HREBSD) methods of determining geometrically necessary dislocation content via cross-correlation promise to be able to produce estimates of the dislocation density of the sample over a larger area with considerably less preparation time and using a much more accessible instrument. However, the accuracy of the new EBSD technique needs more experimental verification, including consideration of possible changes in the specimen dislocation density due to the different preparation methods. By comparing EBSD and TEM dislocation measurements of Electron Transparent platinum specimens prepared using the Focused Ion Beam (FIB), along with EBSD dislocations measurements of specimens prepared by both FIB and mechanical polishing techniques, this paper seeks to verify the accuracy of the new method and identify any changes in the specimens' apparent dislocation density caused by the different preparation processes.

Keywords: scanning electron microscopy, electron backscatter diffraction, transmission electron microscopy, dislocations, focused ion beam, platinum

ACKNOWLEDGEMENTS

This research was partially supported by funding from the U.S. Department of Energy (DOE), Office of Science, Basic Energy Sciences (BES), under award number DE-SC-0012587, Fluke Calibrations with guidance from Rong Ding and General Atomics with oversight from Greg Randall.

I also want to thank Dr. David Fullwood, Zach Clayburn, and the administrators of the BYU's microscopy lab, Dr. Jeffrey Farrer, Michael Standing, and Paul Minson, for their invaluable help.

TABLE OF CONTENTS

ABSTRACT ... ii

TABLE OF CONTENTS ... iv

LIST OF TABLES ... vi

LIST OF FIGURES ... vii

1 Introduction ... 1

2 Background ... 4

2.1 TEM and EBSD ... 4

2.2 Wire Resistivity ... 9

3 Methods ... 11

3.1 Specimen Preparation ... 11

3.2 Scans and Analysis ... 22

3.3 Data Processing ... 28

4 Results ... 30

4.1 Microstructure of Platinum Samples ... 30

4.2 GND Versus Annealing Time ... 33

4.3 Effects of Specimen Geometry and Preparation on EBSD GND Measurements. ... 34

4.4 Comparison of HREBSD and TEM Results ... 38

4.5 Estimating Total Dislocation Density From EBSD Using Curve Fitting ... 43

5 Conclusion 45

References 49

LIST OF TABLES

Table 3.1: Samples and Specimens Prepared 12

LIST OF FIGURES

Figure 2-1: a) Example SEM image of platinum wire, and b) orientation map of the same area generated using EBSD. 5

Figure 2-2: EBSD pattern from scan of platinum wire. 7

Figure 3-1: Image of thin wall FIB section on a platinum wire. Sections to either side of the wall have been removed. 14

Figure 3-2: FIBed sample attached to half-moon grid and cleaned. 15

Figure 3-3: TEM image of thin sample prepared from a 40 μm platinum wire annealed for 2 hours. 18

Figure 3-4: Scanning electron microscope image of thinned specimen prepared from a 40 μm platinum wire annealed for 100 hours. 19

Figure 3-5: Illustration showing cross section of a thinned window and the curved area near the windows base which had to be removed. 20

Figure 3-6: a) STEM image of dislocations in a thinned specimen taken from the 40 μm platinum wire annealed for 2 hours using a HAADF detector and b) counting of the dislocations using a random set of lines overlaid over the STEM image. 23

Figure 3-7: TEM images of hole used in attempt to determine thickness at a) 0°, b) 20°, and c) 40° relative to the hole. 24

Figure 3-8: Cross sectional view of wedge with the point of the wedge towards the top of the paper and the top edge extending to the upper right. This sample had a second thinning process to create a narrower wedge at the top resulting in the ledge midway up the wedge face. 26

Figure 3-9: EBSD pattern on the phosphor screen from a wedge sample. Shadows on the bottom and bottom right show where the screen was occulted, but the cross correlation regions inside the green boxes do not overlap those shadows. 29

Figure 4-1: Mechanically polished specimen IPF orientation maps from a) unannealed 40 µm wire, b) 40 µm wire annealed for 2 hours, c) 40 µm wire annealed for 100 hours, d) unannealed 70 µm wire, e) 70 µm wire annealed for 2 hours, and f) 70 µm wire annealed for 100 hours. 31

Figure 4-2: IPF map of a portion of FIB-prepared wedge taken from an unannealed wire showing the small grain size. 32

Figure 4-3: Graph of average GND measured in the wedge samples with a 0.05 µm step size... 33

Figure 4-4: Graph of average HREBSD measured GND density at 1.2 µm step size for the platinum wire. 34

Figure 4-5: Inverse pole figure of a scans of the 70 µm 2 hours annealed specimens prepared with a) mechanical polishing and b) the FIB. Smearing of the grains is visible in the mechanically polished specimen pole figure. 35

Figure 4-6: a) SEM image of a thin window removed from the 40 µm wire sample annealed for 100 hours, showing the scanned area, b) the grain reference orientation deviation map showing bending in the thin window, and c) The specimen IPF map. 36

Figure 4-7: a) SEM Image, b) GND map and c) Grain Reference orientation map, showing the constant measured GND density across the majority of the wedge and increase and bending at the very tip (towards the bottom of the page.) 38

Figure 4-8: Graph of GND calculated from HREBSD at 1.2 μm step size and the total dislocation density measured in the TEM for different samples. 39

Figure 4-9: Graph of average GND calculated from HREBSD at 1.2 μm step size and the average total dislocation density measured in the TEM. 40

Figure 4-10: Graphs of step size vs calculated GND and the TEM measurements showing agreement between results between 0.05 and 0.1 μm, the approximate spacing for the dislocations as measured by the TEM for a) 40 μm 2hr annealed, b) 70 μm 2hr annealed, and c) 70 μm 100hr annealed platinum wire. 41

Figure 4-11: GND resolution vs step size from Kysar et al. The EBSD resolution assumes an orientation resolution of 0.5° and the HREBSD resolution limit assumes an orientation resolution of 0.006°. Both lines have a slope of 1/L. 42

Figure 4-12: Calculated GND density at different step sizes vs the fit curve from Ruggles et al.'s GND vs step size equation for 40 μm and 70 μm 2 hr annealed wedge samples. 43

Figure 4-14: Predicted total dislocation density from Ruggles' equation vs the total dislocation density measured in the TEM. 44

1 INTRODUCTION

Advances by various groups have resulted in methods to estimate the geometrically necessary dislocation (GND) content of materials from detected distortions of the crystal lattice measured using cross correlation and electron backscatter diffraction (EBSD) techniques [1, 2]. Information on dislocation density and other atomic-scale qualities of materials are traditionally determined using the transmission electron microscope, however the large amount of work required to prepare TEM specimens and the small area available to scan limits the size and number of the samples that can be characterized. Successful TEM specimens for this study took over eight hours to create each, and had final scan sizes of approximately 0.02 μm^2, neither of which is unusual for the TEM [3]. EBSD requires considerably less preparation, uses an instrument that is considerably easier to operate, and can scan much larger areas. As opposed to the 0.02 μm^2 TEM scans used to measure dislocation density, the larger EBSD scans in this study exceeded 1500 μm^2, though larger EBSD scans can reach into the cm^2 [4]. This makes the concept of using EBSD to determine dislocation density an appealing area of study. However, EBSD can only measure the GND content and not the statistically stored dislocation, SSD, content. The net impact on the crystal latticed from SSDs is generally assumed to be negligible, as the distortions cancel each other out over relatively small distances; on the other hand, the distortion from GND add up, resulting in elastic deformation and rotation of the crystal lattice, which are measurable by HREBSD.

Lattice distortion between neighboring points in an EBSD scan is determined using cross-correlation techniques, resulting in an estimate of the net GND content contained within the effective Burgers circuit that is given by the step size of the EBSD scan. As the EBSD step size decreases (thus decreasing the size of the effective Burgers circuit), dipole SSDs are separated and become GNDs, suggesting possible methods for getting access to the total dislocation density. Ruggles et al. presented a relationship between the measured GND density, step size of the scan, and the total dislocation density in the sample. Thus, the total dislocation density could be estimated by fitting the proposed relationship against the experimental curve of GND density vs step size. [5]. If this method proved to be accurate, it would greatly increase the effectiveness of using EBSD as a replacement for the TEM when determining dislocation density.

Up until now, most of the work to validate the EBSD-based approach to GND quantification has used computer simulations. Additional physical testing is needed to verify that the process works correctly [6]. Furthermore, there are open questions relating to the effects of free-surfaces on dislocation distributions, particularly for the thin specimens typically scanned by the TEM [7], which could affect the dislocation density values measured by EBSD and TEM methods.

This study investigates the accuracy of EBSD-based GND quantification by characterizing dislocation content using both TEM and EBSD measurements. It examines GND density vs step size to determine whether the Ruggles hypothesized relationship is accurate, and whether it yields an accurate estimate of total dislocation density. Additionally, it attempts to determine the effects of the different preparation techniques on the resultant dislocation measurements, including the effect of sample thinning, and mechanical vs focused ion beam preparation of samples.

The test bed for the current study uses platinum wire that has been drawn, and then annealed for various lengths of time. Platinum wires used in Resistance Temperature Devices are annealed in order to stabilize their resistivity prior to being shipped to the customers so that the platinum is in a strain free state, and largely free of dislocations which could subsequently recover and modify the resistance. However, the resistivity of the wire fails to stabilize, even after long annealing periods; small changes in resistivity still occur over time, indicating that dislocation density is still evolving. On the one hand, resistance measurements of the Pt wire can be used to indicate dislocation density, as a further check on the results from the microscope techniques; on the other hand, the EBSD and TEM measurements of microstructure might give insights into whether evolution of dislocation density during annealing, or some other effect, such as changes in grain boundary density, contributed to the difficulty in achieving stable resistivity in the wires.

Resistance Temperature Detectors (RTDs) are capable of being used for temperature ranges from -260 °C to 1000 °C. They are generally very accurate devices which are standardized as part of ITS-90. Temperature is determined by comparing the resistance of the device to a reference resistance taken at a known temperature. Platinum is frequently used because it is chemically stable, capable of being drawn into fine wires without being too soft and has a well know change in resistivity with temperature [8].

For the current study, dislocation density measurements were taken of sample wires with a diameter of 40 and 70 μms which were either unannealed or annealed for 2 or 100 hours at 670 °C. These samples and the specimen prepared from these wires and their measured GND and total dislocation density were used to test the accuracy of new methods of determining dislocation density.

2 BACKGROUND

2.1 TEM and EBSD

TEMs have traditionally been used for investigating dislocation content. The curved crystal lattice around dislocation cores passes though the brag condition for the direct beam causing increased diffraction. This can be viewed in a bright field image by looking at the image created by the direct beam, which will show dark lines where the dislocation increased diffraction. Alternatively, the diffracted electrons can be used to create a dark field image where the dislocations will show up as bright lines. Since the dark field image can be created from selected diffracted conditions it can be adjusted to highlight or hide specific dislocations types for identification while the bright field or combined dark field images are better for viewing a complete image of all the dislocations in a sample [3, 9, 10]. In order to follow this approach, specimens must be thinned to electron transparency, generally less than 100 nm [3]; furthermore, they need to have a clean surface finish on both sides, since any damage to the surface may obscure the dislocation lines and make it impossible to get an accurate measurement of dislocation density. The general area viewed with the TEM for finding the dislocation density is frequently 1 μm^2 or less [3]. To determine the density of dislocations, a small grid or set of random lines is overlaid on the image and the dislocation density is found using the equation

$$p = \frac{2N}{Lt} \tag{1}$$

where N is the number of times that dislocations crossed the lines, L is the total length of the lines and t is the thickness of the specimen [11].

EBSD techniques for studying microstructure require much less specimen preparation than the TEM studies since they only need one polished surface, and the specimen does not need to be electron transparent. EBSD can also be used to scan areas several orders of magnitude larger than the TEM can image, resulting in maps of over a cm^2 [4]. See figure 2-1.

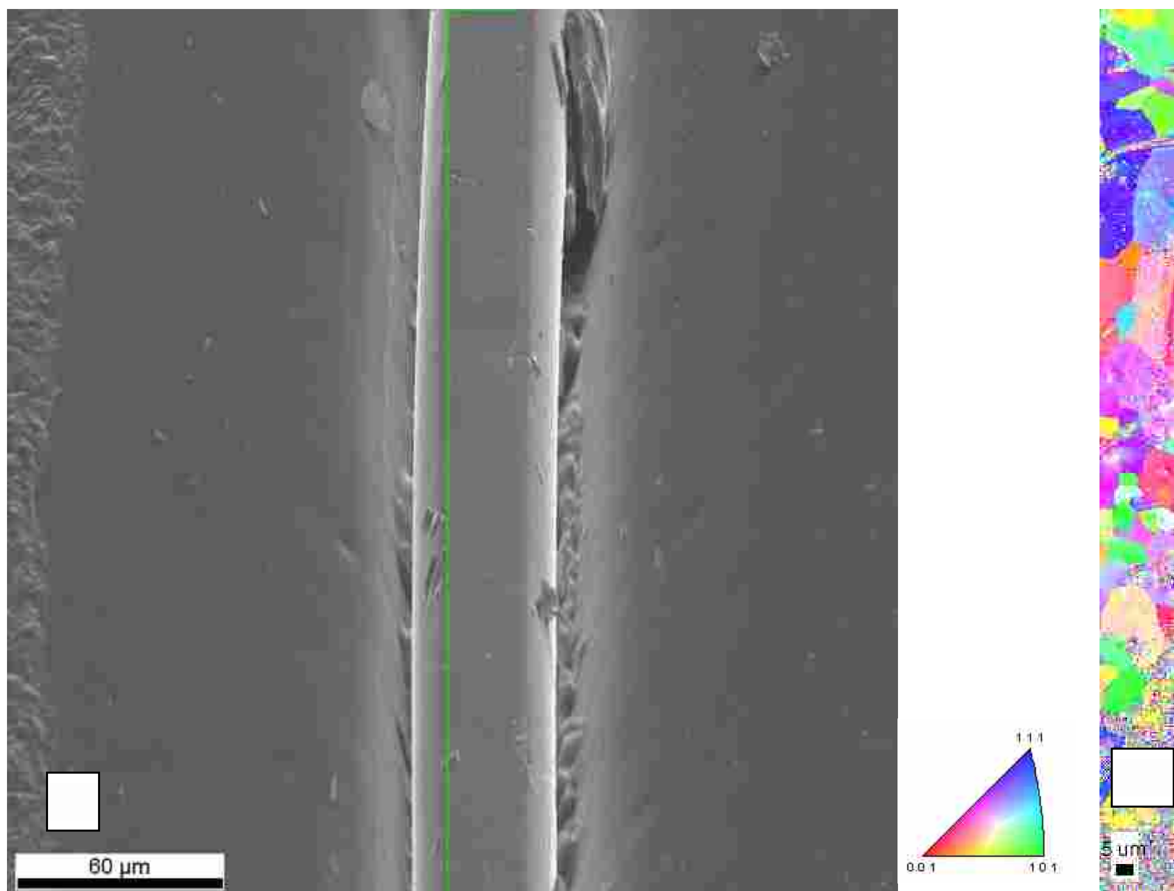

Figure 2-1: a) Example SEM image of platinum wire, and b) orientation map of the same area generated using EBSD.

EBSD determination of dislocation content has been attempted in various ways. EBSD pattern image quality (or equivalent metric used by a given commercial software package) is sometimes used to qualitatively estimate the dislocation density since all dislocations (GNDs and SSDs) are crystallographic defects that negatively affect the electron diffraction and resultant patterns [12]. However, a more quantitative EBSD approach is based upon measurement of lattice distortion caused by geometrically necessary dislocations. The GND dislocation content is typically captured within the Nye tensor,

$$\alpha_{ij} = \epsilon_{nmj}\, \beta_{in,m}, \tag{2}$$

where β is the elastic displacement gradient (encapsulating the elastic lattice distortion), and ∈ is the permutation tensor. Crude measurements of lattice distortion can be made using standard (Hough-based) EBSD [13]. With this method, the equation for the Nye tensors elements becomes:

$$\alpha_{ij} = \epsilon_{nmj}\, \beta_{in,m} = \epsilon_{nmj}\, \omega_{in,m} + \epsilon_{nmj}\, \varepsilon_{in,m} \tag{3}$$

ε and ω are the infinitesimal strain and rotation, respectively. This is approximated as:

$$\alpha_{ij} = \epsilon_{nmj}\, \omega_{in,m} \tag{4}$$

since strain is generally assumed to be negligible, and the standard EBSD method cannot determine ε [14, 15].

Additionally, since EBSD is generally only performed in 2 dimensions, any components of the displacement gradient into or out of the sample (m=3 in the above equation) are unavailable. We end up with 5 measurable values in the Nye tensor and 1 pair that have a known relationship between them [16]. The remaining unknown values are estimated by either taking

the L_1 norm of the known values and multiplying it by the ratio of total Nye tensor values to known Nye tensor values, or by solving for the dislocation density values of each crystal system such that some quantity such as elastic energy is minimized (which can be computationally expensive) [17].

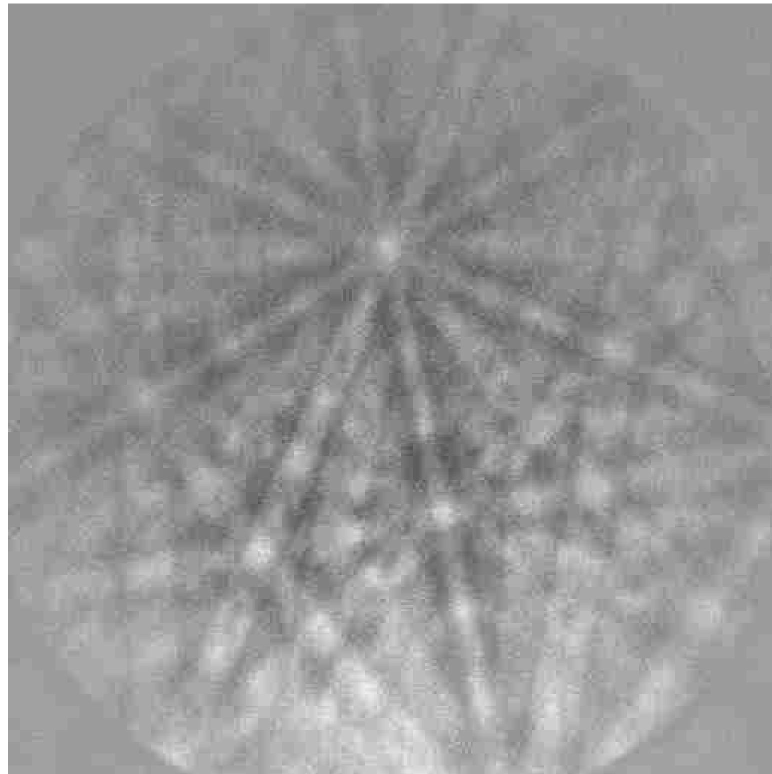

Figure 2-20: EBSD pattern from scan of platinum wire.

More advanced methods of determining use a cross-correlation approach, sometimes known as high-resolution EBSD (HREBSD). Subtle changes in the diffraction pattern between neighboring points are detected using fast Fourier transformation convolutions in order to determine accurate strain and rotation gradients allowing it to use the a more accurate β tensor

including ε in determining α [14] [18]. Compared to the 1-0.5° available with a Huff transform HREBSD can have an accuracy of ~0.003° [6, 18].

Since the EBSD method is based only on the lattice distortion created by GNDs it cannot detect those dislocations which cancel out each other's distortions (SSDs) and therefore cannot normally determine the total dislocation density. However, as the step size of the scan decreases dislocations that were previously statistically stored are separated, resulting in a higher net GND content, as defined by Burgers circuits given by the EBSD step size. If the continuum theory relating lattice distortion to GND content were still valid when examining single dislocations (currently an open question in this area of study), then theoretically at small enough step size, every dislocation would become a GND, allowing the EBSD technique to detect all dislocations, potentially limited only by the microscope's spatial resolution [5].

Additionally, computer models developed by Ruggles et al. predict that the relationship between measured GND content and step size $\bar{\rho}_m(L)$ can be approximated by the following equation:

$$\bar{\rho}_m(L) \approx \frac{\sqrt{2\rho_t}}{L\sqrt{\pi}}\left(exp\left(\frac{-\rho_n^2L^2}{2\rho_t}\right) - \frac{1}{erfcx\left(\frac{\rho_nL-q}{\sqrt{2\rho_t}}\right)}\right) + \rho_n erf\left(\frac{\rho_nL}{\sqrt{2\rho_t}}\right) \quad (5)$$

where L represents the step size, ρ_t represents the total dislocation density, ρ_n represents the net dislocation density, and q represents the maximum amount of detectable lattice distortion between patterns divided by the magnitude of Burgers vector. If a fine scan is taken, and the EBSD patterns are saved, by skipping points in the analysis it is possible to evaluate GND content over a range of different step sizes using a single scan. Curve matching this equation to

the resulting data, the values of ρ_n, q, and most importantly ρ_t can be estimated allowing us to predict the total dislocation density from the GND density [5].

2.2 Wire Resistivity

As mentioned, the test bed for the current study uses Pt wires from Resistance Temperature Detectors (RTD). The majority of metals have higher resistance at higher temperatures, with the exact rate of change varying depending on the metal and temperature. Platinum's resistance to temperature relation is well known and can be approximated by the Callendar–Van Dusen equation as

$$R_t = R_0[1 + At + Bt^2] \tag{6}$$

where R_0 is the resistance at 0 °C, Rt is the resistance at the measured temperature, t is the temperature in °C and A and B are constants equaling $3.9083 * 10^3 (°C^{-1})$ and $-5.7750 * 10^{-7} (°C^{-2})$ respectively [19]. The temperature sensors are frequently made by coiling the platinum wire into a helix and then wrapping that helix around a quartz core before sealing it in a protective case [20].

Dislocations and grain boundaries can also increase the resistance of a metal. This occurs because dislocations act to scatter the electrons as they flow through the material decreasing their mean free path [21]. This extra resistance increases proportionally with the dislocation density. The total resistivity can be modeled as

$$\rho = \rho_d + \rho_p + \rho_i + \rho_{gb} \tag{7}$$

where ρ is the total resistivity, ρ_d is the resistivity due to dislocations, ρ_p is the resistivity due to phonos, ρ_i is the resistivity due to point defects, and ρ_{gb} is the resistivity due to grain boundaries. The dislocation resistivity can then be modeled as

$$\rho_d = R_d N \tag{8}$$

where N is the dislocation density and R_d is a specific resistivity, which B. R. Watts gave as $3.6 * 10^{-25}\ \Omega\ m^3$ in his paper on conduction electron scattering in dislocated metals [22]. This relationship will be used to estimate the impact of annealing on the dislocation density of the wires used in the following study.

3 METHODS

3.1 Specimen Preparation

Three separate sets of specimens were prepared for this study: i) a set of electron transparent specimens, prepared by focused ion beam lift-out approach, that could be analyzed in the TEM to count the number of dislocations; ii) a set of sharp wedge-shaped specimens, also cut via FIB, for a direct comparison of EBSD against the TEM for similarly prepared specimens, and to observe any change in properties with specimen thickness; and iii) a set of mechanically polished specimens, to measure the dislocation density measured from the EBSD using standard EBSD specimen preparation techniques. The specimens were also used to attempt to observe any changes in dislocation density of the platinum with different annealing times. Table 1 lists the set of specimens that were examined.

The mechanically polished and FIB produced wedges were prepared for both the 40 μm and 70 μm wires for unannealed samples and for samples at two annealing times. Due to the difficulty in preparing the electron transparent specimens for the TEM, and their fragility, fewer samples were studied. Specimens for each of the 3 annealing times for the 70 μm wire were produced in order to observe the effect of the annealing on the dislocations; and one specimen of the 40 μm wire, after 2 hours of annealing, was prepared for TEM, in order to observe any differences caused by wire size.

Table 3.1: Samples and Specimens Prepared

	Unannealed	2 hr annealed	100 hr annealed
40 μm wire	Mechanically Polished FIBed Wedge	Mechanically Polished FIBed Wedge TEM Window	Mechanically Polished FIBed Wedge
70 μm wire	Mechanically Polished TEM Window	Mechanically Polished FIBed Wedge TEM Window	Mechanically Polished FIBed Wedge TEM Window

The time-intensive part of this process involved preparing electron transparent specimens which could be used in the TEM. Multiple methods for preparing metallic TEM specimens exist with different advantages and disadvantages. One of the more common is to cut off 100 to 200 μm thick slices of a bulk sample with a lapping saw, or via spark erosion, and then use a punch to create a 3mm diameter disk that will fit in the transmission electron microscope. This disk can then be thinned by dimple grinding or by electro polishing, which uses a constant stream of acid and an electric current to wear away the specimen material until a small hole appears. The area around this hole should be thin enough to scan in the transmission electron microscope. The advantage of this system is that the electric polishing creates little to no mechanical damage in the sample, but was impractical for preparing specimens from the thin wires used in this study [3].

Another potential method uses an ultramicrotome. With ultramicrotomy the sample is set in epoxy and then cut into slices approximately 100 nm thick or less with a fine glass or diamond knife [3]. When attempted, the specimens from the platinum wire samples would quickly curl out of the thin epoxy due to poor adhesion between the wires and the surrounding matrix, and

because of the residual stress in the wire. Additionally, there was some concern that the knife could have introduced new dislocations into the specimen as it cleaved it.

A third method is to use a Focused Ion Beam (FIB), with the FIB lift out method. In this method a FIB attached to a scanning electron microscope uses high energy gallium ions to cut a small wall from the sample that can then be attached to a TEM sample-holding grid. Then the specimen is thinned to electron transparency by using the ions to sputter away one or both faces of the wall [3, 23]. This method is frequently unavailable since the focused ion beam is a very expensive piece of equipment compared to the previously mentioned methods, but Brigham Young University has a FIB available for use. The advantages of allowing tiny specimens to be taken from specific locations on the sample, made this the best choice for this study since it allowed us to pull the specimens form the narrow platinum wire [3]. Apart from the cost of the equipment needed for FIB specimen preparation, other downsides are the complexity of the process and possibility of amorphizeing the surface layer of the specimen as the ions deposit their energy into the material [23]. However, unlike the problems mentioned for the other methods, these ones could be practically overcome; in fact, the specimens prepared with the FIB were found to produce very good surfaces for getting patterns when used for EBSD.

For the FIB process the platinum wires were attached to a piece of carbon tape, and then the FIB was used to deposit a protective layer of platinum approximately .5 μm thick over the area of interest. This was done by inserting a small hollow needle connected to a source of platinum containing compound. As the platinum compound was injected into the space above the specimen, a low-current ion beam was used to crack the platinum-containing molecules which then adhered to the surface of the sample. This layer of platinum served two purposes. First it helps protect the specimen from the ion beam, and second since the ion beam mills

preferentially on angled surfaces, the platinum cap creates a smooth surface that can be milled uniformly [24]. The FIB was then used to mill away the material on both sides of the area of interest, creating a wall approximately 2.5 µm thick. See figure 3-1.

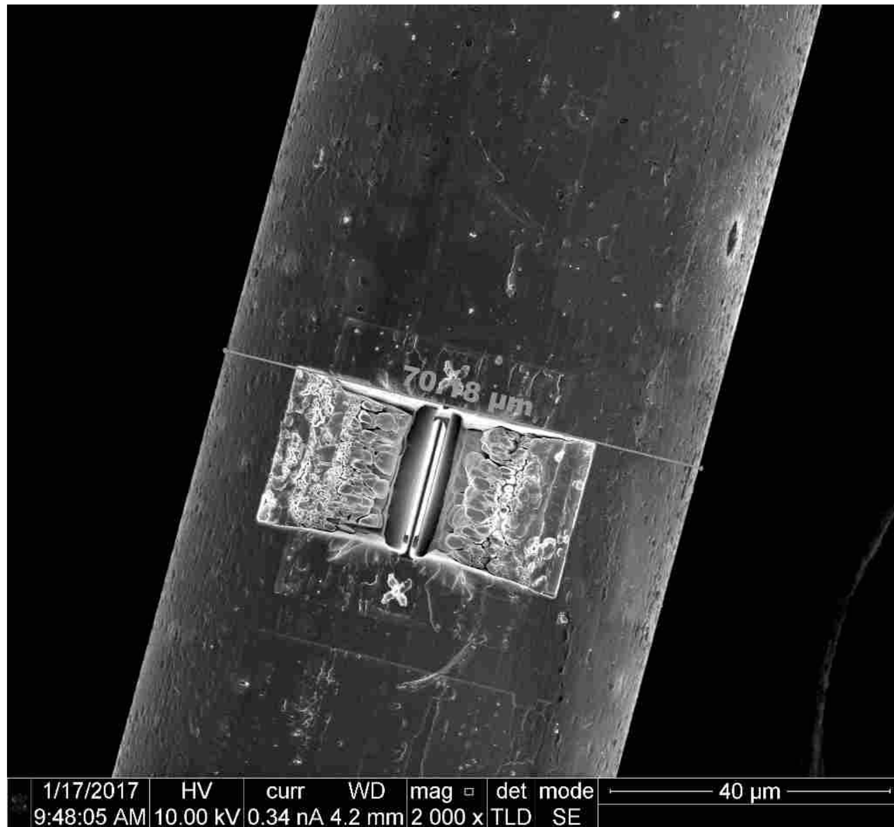

Figure 3-1: Image of thin wall FIB section on a platinum wire. Sections to either side of the wall have been removed.

After milling the wall, the specimen was tilted to 52° and the sides and base of the wall were milled away leaving only a small bridge holding the specimen to the wire. A small needle known as an Omni-probe was then lowered to just above the specimen, and the FIB was used to apply a small amount of platinum connecting the specimen to the needle. Following that, the

small bridge connecting the specimen to the rest of the wire was cut using the FIB. Care had to be taken to prevent platinum from the platinum deposition needle from leaking through the needle during this process. Despite closing the valve, enough platinum would bleed through the closed valve to partially reconnect the specimen to the bulk sample as the fib attempted to cut it away. Removing the platinum deposition needle prior to cutting the connecting bridge would cause significant vibrations ripping the specimen from the Omni-probe so instead, the platinum deposition source heaters were turned off and the platinum source was allowed to cool prior to cutting. Once the bridge was cut the Platinum needle could be removed and the specimen lifted off of the wire. The specimen was then moved over to a copper half-moon grid and attached using more deposited platinum, before again cooling the platinum source and cutting the specimen off of the Omni-probe. See figure 3-2.

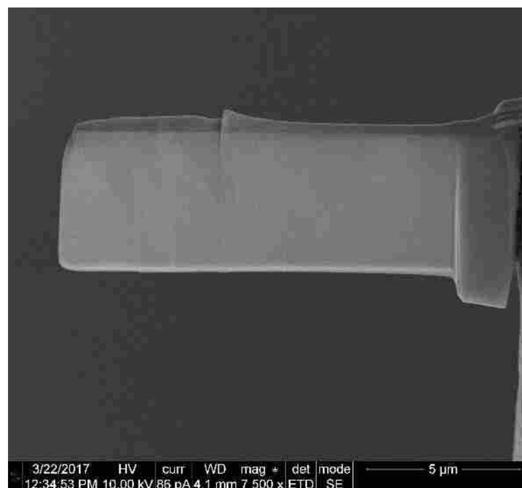

Figure 3-21: FIBed sample attached to half-moon grid and cleaned.

Once the specimen was attached to the half-moon grid it was tilted 1.5° from level and the front surface was milled with a cleaning cross-section (which refers to a milling pattern where instead of milling the entire area at once, one edge of the area is completely milled down, and then the ion beam moves forward creating a clean cross-section as it goes, not a change in the beam voltage or current). This produced a clean face by removing any material that may have accumulated on it during previous steps. The specimen was then tilted 1.5° from level in the other direction and the process was repeated to clean the back side. These tilts counteracted the cone shape of the ion beam, which would normally create an angled surface since the ion beam is wider at the top of the specimen than at the bottom, to produce parallel faces on the two sides of the specimen. Additionally, milling at such a shallow angle helped reduce the amount of damage the ion beam did to the specimen by helping ensure that the ions only penetrated into the very outside layer of the specimen [25].

The specimen then had to have an electron transparent window milled into it by using the ion beam to gradually thin a section of it from the initial 2.5 μm to approximately 100 nm, while leaving a ledge below the window to provide structural support. In order to retrieve useful information in the TEM, electrons traveling through the specimen should pass through without a significant number of the electrons interacting with the specimen material multiple times. If the specimen is too thick, then large amounts of electrons will have multiple interactions with the atoms in the specimen, degrading our ability to gather information from those electrons [3]. Numerical calculation of the mean free path of electrons through the sample, and the corresponding maximum specimen thickness can be difficult since the answer varies with the atomic number, the angle and type of scattering, and the wave function and frequently requires numerical methods to solve for high atomic number atoms [26]. Even then, the produced

numbers can be off by an order of two [3]. Due to the difficulty and imprecise nature of these calculations, a general rule of 100 nm or less is frequently used, with thinner being better but harder to produce [3].

While it may be possible to obtain a value for the mean free path that is close to the actual value of platinum using these calculations, hitting an accurate target thickness for an electron transparent specimen is impractical due to the inability to accurately measure the thickness of the specimen while it was in the SEM. Instead, empirical tests using indicators of electron transparency during the milling process, and in the TEM, were applied to determine when the specimen reached electron transparency. By putting a specimen in the TEM and focusing the Electron beam on a small area of the specimen, the amount of scattering could be observed as a cone of scattered electrons on the phosphor screen around the direct beam, with the brightness of the cone compared to the direct beam giving an indication of whether the specimen was thin enough to produce useful data.

Prior to this final test, and during the milling process, two indicators were found to be useful for determining when the specimen was thin enough to be used in the TEM. As the specimen reached electron transparency some of the electrons used to observe the specimen in the SEM began to pass through the specimen instead of interacting and generating secondary electrons, leading to a slight change in contrast. With careful observation, this could be used as a signal that the specimen was electron transparent. Additionally, since the beam was slightly off of parallel to the back surface, and small curvatures developed in the thin wall as it was milled, it was found to be possible to take multiple small cuts from the window with the ion beam until a small perforation appeared, producing extremely thin specimens. See figure 3-3.

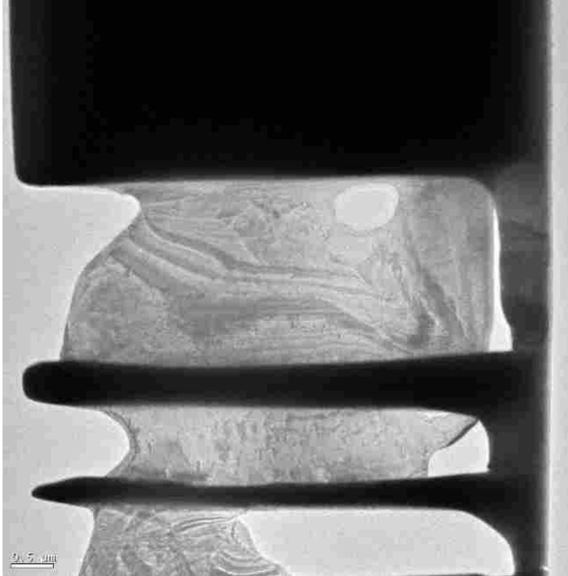

Figure 3-22: TEM image of thin sample prepared from a 40 µm platinum wire annealed for 2 hours.

Because the aperture of the ion beam was constantly being milled which would alter the beam current, settings for the beam had to be adjusted each time. A current of approximately 26 pico amps at 30 kV was found to be a good general setting but cutting depth (dwell time) settings had to be adjusted for each session. To find the correct settings several small thin areas were prepared towards the left side of the specimen. The specimen and milling process were carefully observed during this process in order to reach electron transparency without cutting through the small test area. These cuts were repeated until correct settings were found that allowed the production of a small electron transparent area while leaving a ledge at the base of the specimen for structural stability. Due to the tendency for the support ledge to become thinner near the middle of larger windows, the correct settings for the small test area were ones that produced a thicker ledge than would be needed for the final larger window. Once the correct settings were

found for that session, the large electron transparent area was milled near the center of the specimen. See figure 3-3 and 3-4.

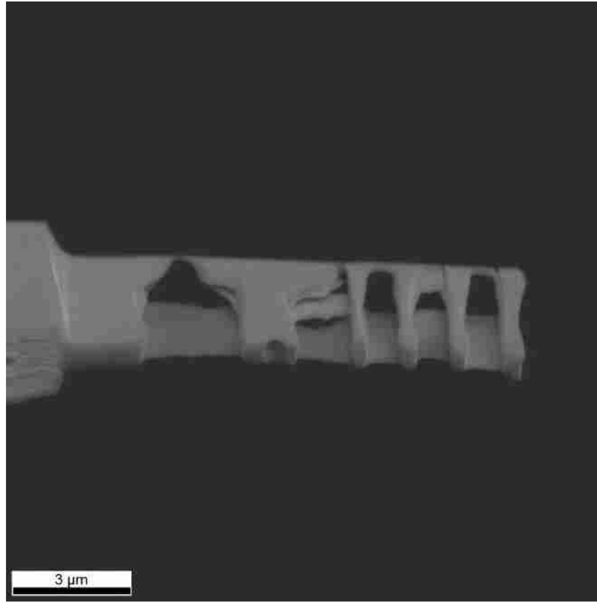

Figure 3-23: Scanning electron microscope image of thinned specimen prepared from a 40 μm platinum wire annealed for 100 hours.

Areas of the specimen outside of the beam often still appeared to be milled, especially the bottom ledge, likely due to the removed platinum atoms acting like an ion beam themselves. This resulted in the requirement for a larger initial ledge than would have been needed in the absence of this effect. Additionally, the front face of the window frequently developed a concave curve as it approached the ledge resulting in thickening of the window near its base, which would have made a large section of the window too thick to use in the TEM. See figure 3-5. In order to remove this curve and create more parallel front and back surfaces of the window, multiple cutting steps were taken instead of the normal single cutting step. Between each step the top

edge of the milling area (the part that created the final surface of the window) was moved slightly further in towards the window and the bottom edge of the milling area (the part furthest from the face of the window) was moved in towards the window face significantly. This resulted in more significant milling of base of the window where it contacted the ledge than the rest of the windows face, removing the concave curve that was causing the extra thickness.

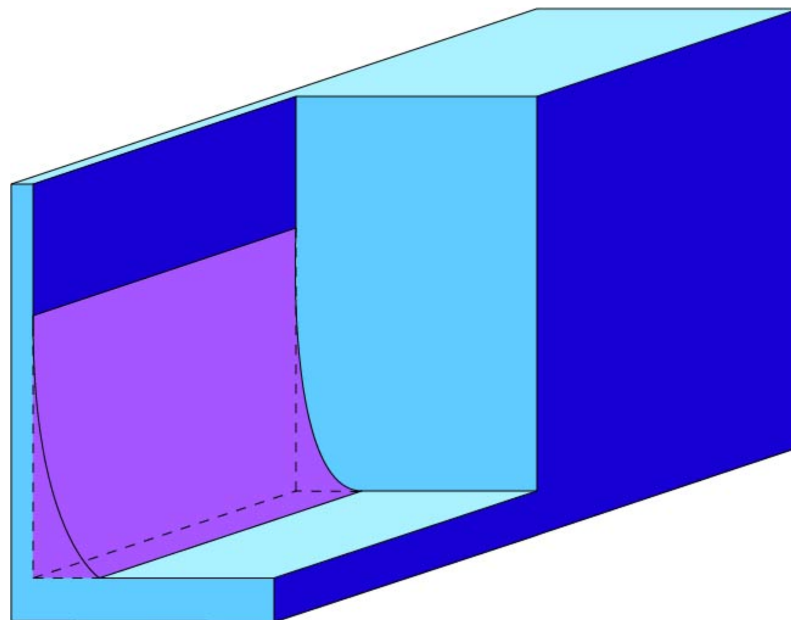

Figure 3-24: Illustration showing cross section of a thinned window and the curved area near the windows base which had to be removed.

While the FIB mills the surface of the specimen, the ions also create a thin amorphized surface layer up to several tens of nanometers thick. Normally this is removed by using briefly milling the specimen with the FIB at a lower voltage than that used for cutting (5 KV instead of 30 KV) or by placing the specimen into the ion mill which can be more gentle than the FIB, but

is harder to monitor and requires additional temperature controls. The lower energy ions mill away the amorphized layer left by the initial thinning of the window, and since they penetrate less deeply into the specimen the new amorphized layer they create should be considerably thinner [25]. However, in tests with both the FIB and the ion mill, this approach made it difficult to reliably achieve an electron transparent specimen without milling through the specimen. When the specimen was thinned close to electron transparency the lower imaging resolution available at the lower FIB voltage would usually result in cutting completely through the thin window; on the other hand, if the window was made thicker and then thinned with lower voltage FIB settings or the ion mill, the longer duration milling would result in extra damage to the specimen surface. Since the curvature which developed in the window would often hide parts of the surface this would not uniformly effect the entire window surface, and could result in inaccuracies when comparing scans, so it was skipped. Additionally, the thin amorphous layer aided in focusing the TEM leading to better imaging, without drastically reducing the ability to observe the dislocations.

The thin wedge platinum specimens were prepared using the same method used to prepare the electron transparent specimens, except they were tilted in the opposite direction during cleaning in order to produce a sharp wedge and the final thinning step was omitted. Once the wedge shape was milled, multiple cleaning cross-sections were used perpendicular to the wedge in order to produce a flat cross-section. This created an approximately 5 μm tall wedge with a peak angle of approximately 6°. This specimen was thick enough across the majority of its surface area to act like the bulk specimens usually used in EBSD, but was prepared with a similar method as used for the electron transparent window, allowing us to observe what effect this preparation technique had on the EBSD GND measurements. Additionally, because of the

sharp angle of the wedge, we hoped to be able to observe any change in the GND measurements as we approached the wedges tip, which would have given us insight into how the reduced thickness in electron transparent specimens affected the dislocation density (for example, by dislocations escaping from the free surfaces).

The mechanically polished specimens were prepared in a manner typical of EBSD specimens, albeit with the complication of the wires being extremely thin. This let us compare them to the specimens prepared by the FIB to see if there was any significant change in the actual or apparent dislocation density due to the different type of polishing. Furthermore, other microstructural details (such as grain size) could be observed due to their larger size. The specimens were prepared by first embedding the wires in an epoxy puck and then hand polishing using 240, 320, 400, 600, 800, and 1200 grit silicon carbide abrasive disks followed by 1 μm and 0.3 μm alumina, and finally 0.05 μm colloidal silica. As the specimens were polished, they were checked between each pass to make sure that they had not worn through the thin platinum wire. The surface of the pucks, where the wires were not exposed, was painted with conductive silver paint to reduce charging. Finally, the entire surface was coated with a 150 angstroms thick layer of carbon using a thermal evaporation physical vapor deposition technique to create a conductive layer connecting the wires to the paint.

3.2 Scans and Analysis

The electron transparent specimens were placed in the TEM and imaged using Scanning Transmission Electron Microscopy with a High Angle Annular Dark Field (HAADF) detector at 220 mm, 500 mm and 70 mm camera lengths in order to image the dislocations. The Annular Dark Field produced the best results by allowing us to combine the images from multiple dark

field conditions into one high contrast image, and by allowing us to change the camera length which changed the Z vs Bragg angle contrast [3], so that multiple settings with different levels of Bragg angle contrast could be compared to aid us in identifying which features were dislocations. These dislocation images were overlaid with a randomized set of lines and the number of intersections of the dislocations with the lines were counted and compared to the total length of the lines to determine the dislocations per area of the specimen. See figure 3-6.

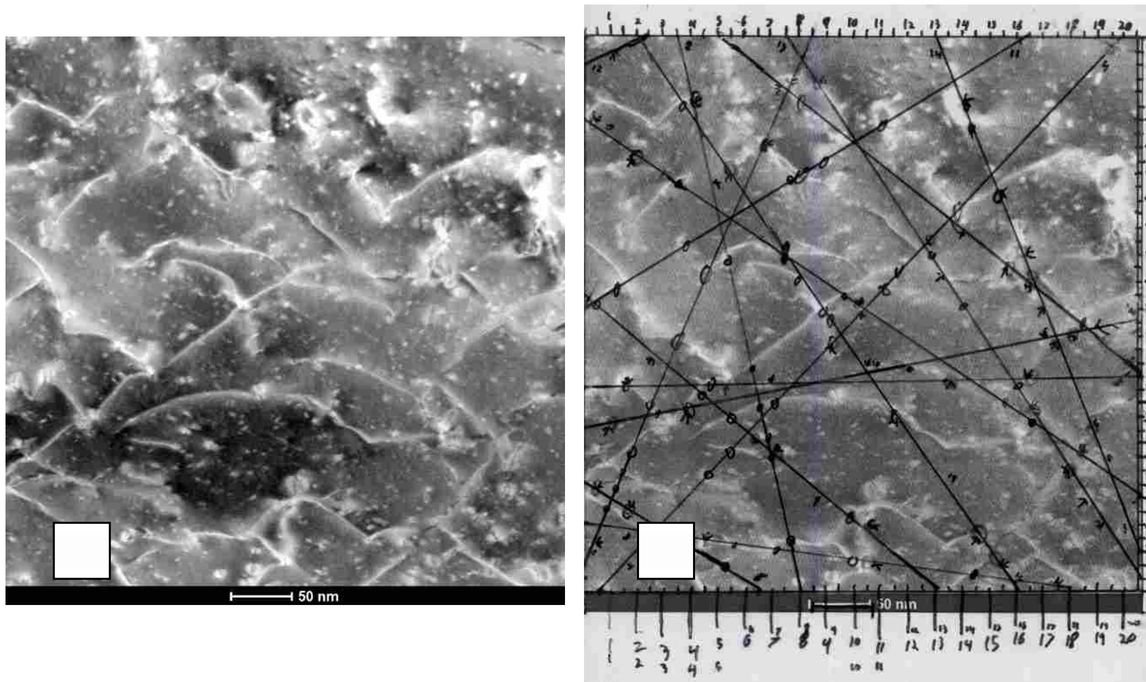

Figure 3-44: a) STEM image of dislocations in a thinned specimen taken from the 40 μm platinum wire annealed for 2 hours using a HAADF detector and b) counting of the dislocations using a random set of lines overlaid over the STEM image.

Equation 1 also requires the thickness of the specimen to determine the density of dislocations per volume [11]. Accurately measuring the thickness of such a thin specimen is difficult, and multiple methods exist to attempt to find it. One attractive method is to image the

specimen from the top down in the SEM and then simply measure the thickness of the window in the image, however small amounts of curvature in the thin window made this technique unusable for our specimens, since the distance between the different parts of the curve, when viewed from above, was significant compared to the total thickness of the window.

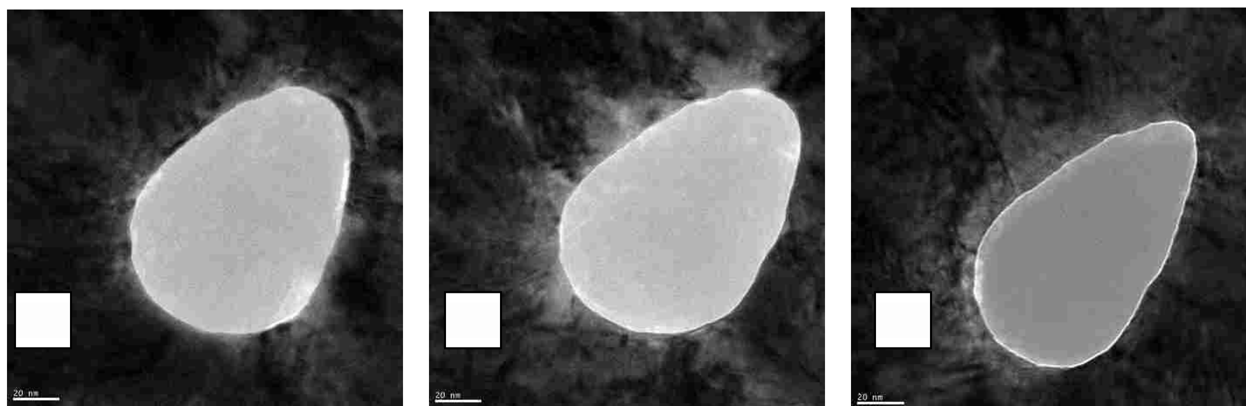

Figure 3-90: TEM images of hole used in attempt to determine thickness at a) 0°, b) 20°, and c) 40° relative to the hole.

Physical markers are another method that can be used to measure the thickness of the specimen. By creating markers in line with each other on either side of the thin window, and then tilting the specimen and observing the new projected distance between the two markers the thickness could be calculated from simple trigonometric functions. The two types of physical marker that were considered included pairs of carbon deposits caused by the electrons in the TEM breaking carbon containing molecules which would adhere to the surface, and holes milled through the window with the FIB. The carbon deposition rate in Brigham Young Universities TEM was found to be insufficient to create these carbon markers while the holes produced by the

FIB tended to have a curved upper rim which concealed the location of the top of the hole. See figure 3-7.

The method to determine thickness that was eventually settled on used Electron Energy Loss Spectroscopy (EELS) to find the percentage of electrons that undergo inelastic scattering in the specimen, which relates to the specimen thickness. As the thickness of the specimen increases the fraction of the electrons that undergo inelastic scattering events increases, and by comparing the ratio of electrons that passed through without losing energy (the area under the zero loss peak, I_{in}) to the the electrons that lost energy through inelastic interactions (the area under the plasmon peak I_0), to the mean free path of electrons through the sample material, the thickness of the specimen could be determined from the equation

$$t = \lambda \, ln\left(\frac{I_{in}}{I_0} + 1\right) \tag{9}$$

where t is the thickness of the specimen and λ is the mean free path [27]. This method had several advantages that made it the method of choice for this study including that was relatively fast to gather the EELS data, and the information could be handled by the computer. However, it required knowledge of the mean free path, which as stated above can only be roughly estimated theoretically, and if measured experimentally is likely to be inexact as explained below. Luckily this method is only marginally effected by inaccuracy since an error in determining mean free path should affect all specimen measurements proportionately. This means that even if there was an error in determining the mean free path, the data would be valid when comparing between samples.

Since the mean free path in equation 9 is dependent on the scattering angles picked up by the microscope detectors, it is a unique value for each microscope setup. Due to this and the

difficulty and inaccuracy of theoretical models we used empirical methods to measure the mean free path. With the wedge specimens we were able to measure not just $\frac{I_{in}}{I_0}$ in the microscope, but also were able to estimate thickness in the SEM, giving us two of the 3 unknowns in equation 9.

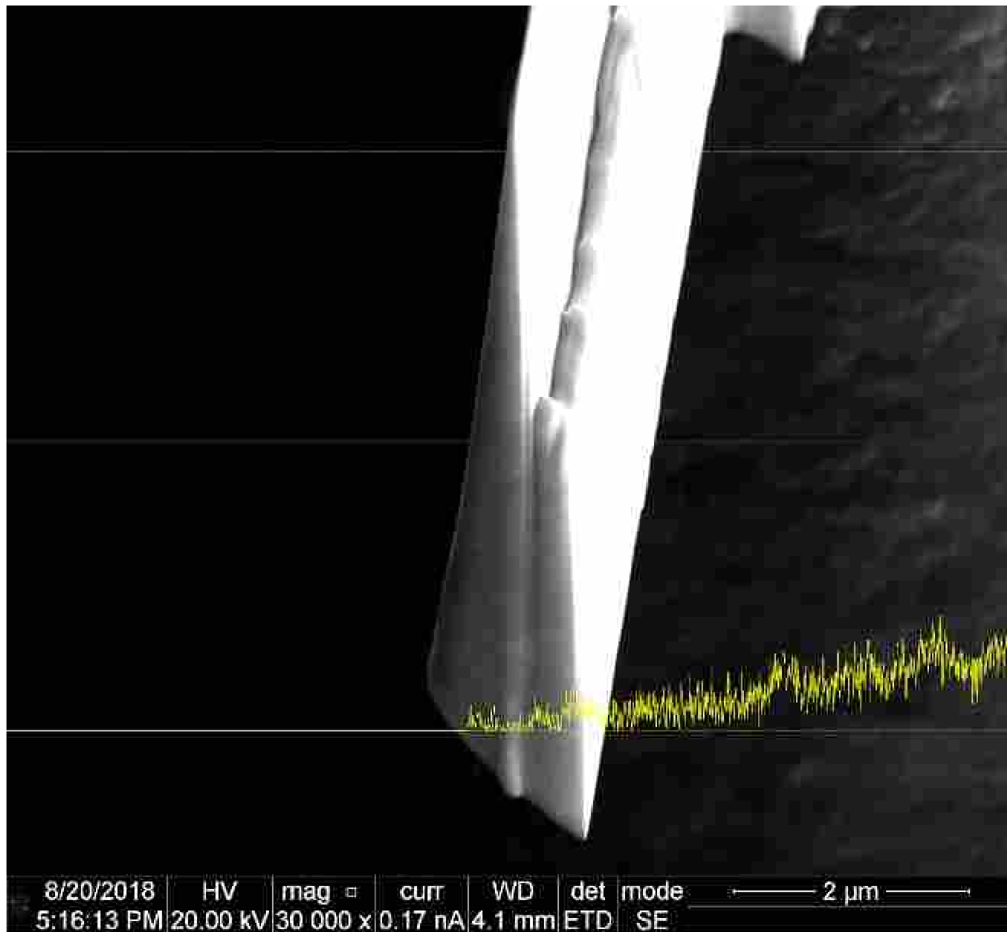

Figure 3-91: Cross sectional view of wedge with the point of the wedge towards the top of the paper and the top edge extending to the upper right. This sample had a second thinning process to create a narrower wedge at the top resulting in the ledge midway up the wedge face.

To determine the thickness of the wedge it was placed in the SEM and tilted to 45° to make the cross-section visible and rotated by 5°, making the top edge visible, to make it easier to

locate the point of the wedge cross section. See figure 3-8. The thickness of the wedge in the image at a measured distance from the peak was measured and divided by cos(5°) to find the thickness, and the distance from that point in the image to the tip of the wedge was measured and divided by cos(45°) to find the slope of the wedge, and thus it's thickness at any point along it. This assumed that the wedge had a constant slope along its height, which was hard to verify in the thinner portion of the wedge, but since as mentioned above any errors arising from this should have proportional effects for each specimen this was not considered to be a serious problem.

An EELS spectrum of one of these wedges was taken at a location which was 0.3 μm thick, and the mean free path of the electrons through platinum calculated by using equation 9 rearranged to solve for lambda:

$$\lambda = t \Big/ ln\left(\frac{I_{in}}{I_0} + 1\right) \tag{10}$$

resulting a mean free path value of $\lambda = 0.12$ μm. This then allowed us to use EELS to measure the thickness of the electron transparent specimens.

All of the wedge and mechanically polished specimens were scanned using EBSD, along with the thin window specimens from the wires annealed for 2 hours. Each specimen was placed in the scanning electron microscope and tilted to 70° and scanned with a 20 kilovolt beam on an FEI S-Feg XL30 scanning electron microscope with a TSL EBSD detector at a 0.05, 0.15, and 0.2 μm step size. The resulting data was analyzed using cross correlation to determine the GND content of the specimen [28].

3.3 Data Processing

The mechanically polished and wedge specimens prepared on the fib had significantly different EBSD results. The wedge specimens showed a problem with occultation of the phosphor detector. While the thinned wedge area was cut out of the lifted wall, there was still an area of thicker wall next to the wedge. Additionally, the wedge was attached to a copper half-moon grid, which was in turn attached to a FIB grid holder. All of these protruded above the surface of the wedge and could have occulted backscatter electrons from part of the phosphor detector.

OIM analysis interpreted the edge of this shadow as another Kikuchi diffraction band and attempted to use it in the analysis. This lowered the confidence index (i.e. the confidence of the software that the selected orientation associated with a given pattern is correct) of all the wedge specimens, since the extra line created alternative crystal orientation solutions; for some points the issue caused incorrect orientations to be identified. By manually inspecting the data, it was determined that requiring a minimum confidence index cutoff of 0.2 filtered out the incorrect orientations while retaining most of the points with correctly identified orientations; variations in pattern quality between specimens required small adjustments to the confidence index cutoff in some cases.

However, unlike the OIM analysis, the region of the pattern used for cross correlation by HREBSD was centered near the middle of the image and missed the lines created by the shadows of the wedges' supports. See figure 3-9. Hence, no further filtering of the data points was required specifically for HREBSD.

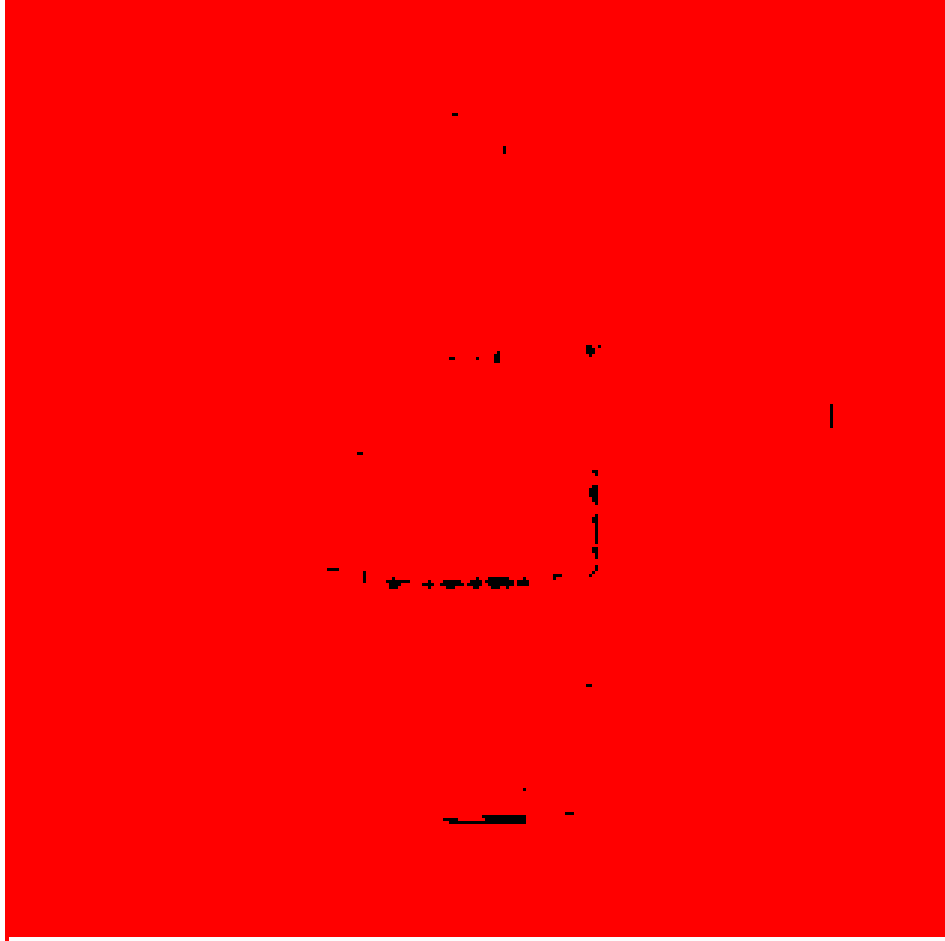

Figure 3-99: EBSD pattern on the phosphor screen from a wedge sample. Shadows on the bottom and bottom right show where the screen was occulted, but the cross correlation regions inside the green boxes do not overlap those shadows.

When performing EBSD on very thin specimens (such as when using Transmission Electron Backscatter Diffraction) it would be wise to be aware of the additional geometry used to support the specimen and how it can negatively affect the patterns.

4 RESULTS

4.1 Microstructure of Platinum Samples

Figure 4-1 presents inverse pole figure (IPF) orientation maps of the mechanically polished specimens. The mechanical polishing approach yielded much larger scan areas compared to the FIB preparation methods, resulting in more representative analyses of grain structure for the different materials. As expected, grain size decreased as annealing time went up. Based on the EBSD measurements, the 40 μm and 70 μm unannealed wires had average grain sizes of 0.39 μm and 1.29 μm respectively. Note, these are measured via equivalent circle diameter and do not fully address the shape of the grain, as will be discussed below. The two hour annealed 40 and 70 μm specimens had grain sizes of 13.89 and 13.03 μm respectively, and the 40 and 70 μm specimens annealed for 100 hours had grain sizes of 18.10 and 28.16 μm. However, for all specimens except the unannealed specimens, many of the grains were in contact with the boundary of the polished area, making the grain size estimate a minimum size, rather than an accurate average value.

As mentioned above, the grain size numbers did not adequately describe the unannealed grains, due to their geometry. As can be seen in figure 4-2 d, and in figure 4-3, the grains are heavily elongated in one dimension. The grains of the unannealed samples had a relatively consistent minimum dimension, with an average value of 0.34 μm, which is not captured by the equivalent circle diameter analysis. The mechanically polished 40 μm wire specimen was

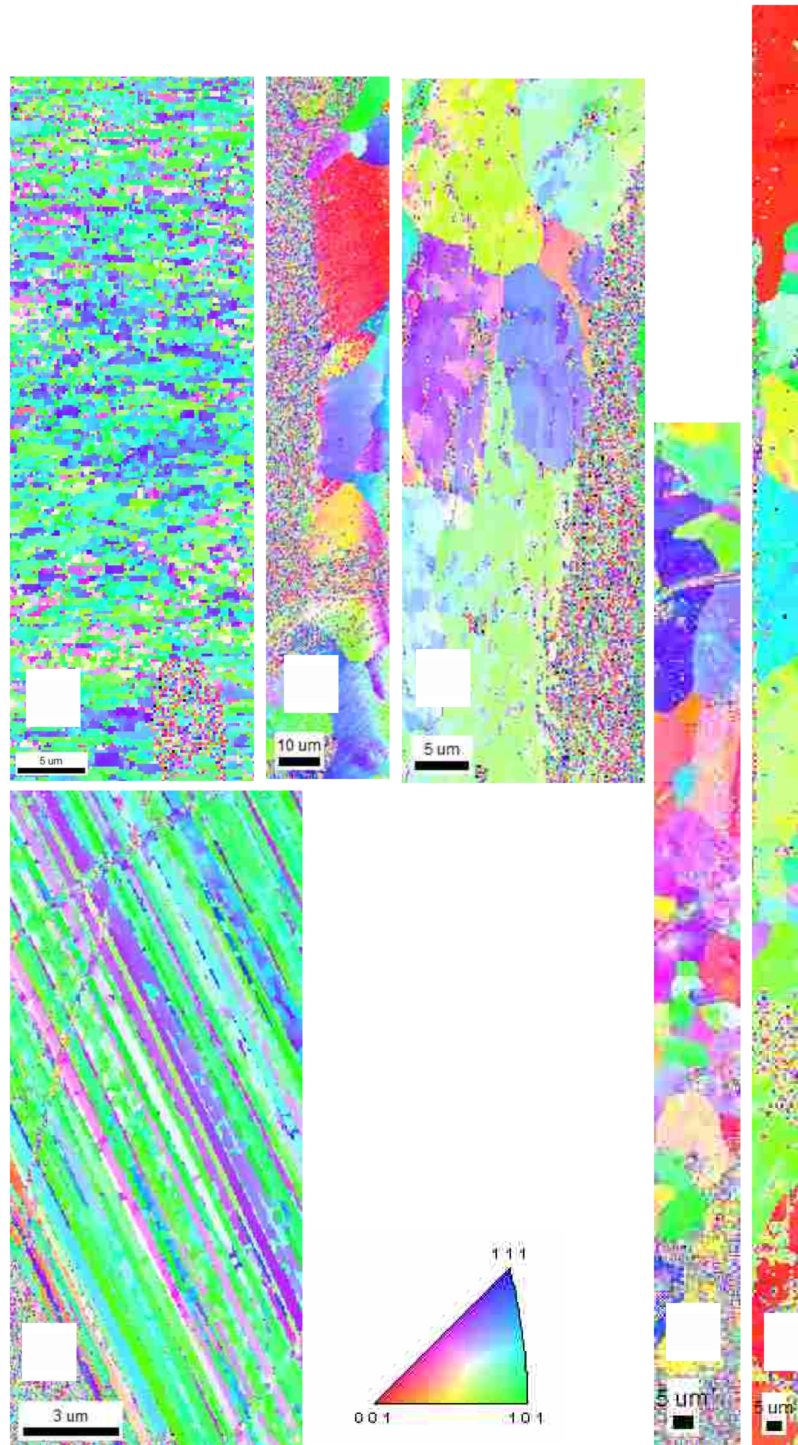

Figure 4-10: Mechanically polished specimen IPF orientation maps from a) unannealed 40 µm wire, b) 40 µm wire annealed for 2 hours, c) 40 µm wire annealed for 100 hours, d) unannealed 70 µm wire, e) 70 µm wire annealed for 2 hours, and f) 70 µm wire annealed for 100 hours.

polished across the face of the wire resulting in almost circular grain cross sections with a radius close to the grains' minimum dimension, while the mechanically polished 70 µm wire specimen was polished along the length of the wire showing the elongated grains. See figure 4-1 (a) and 4-1 (d). The wedge specimen from the 40 µm wire also shows the elongated dimension. See figure 4-2.

Figure 4-11: IPF map of a portion of FIB-prepared wedge taken from an unannealed wire showing the small grain size.

4.2 GND Versus Annealing Time

As discussed earlier, the step size used in the HREBSD analysis of the GND content represents the size of a virtual Burgers circuit; the distortion between lattice structures of points separated by the given step size is used to determine the Nye tensor, and related GND content. Measured GND content is highly dependent upon the assume Burgers circuit size / step size. Analysis is typically applied at step sizes that are representative of the GND structure size – usually assumed to be of the order of a micron [5, 29]. However, due to the small size of the unannealed specimen grains, the larger Burgers circuits cannot be used (there are no neighboring points in the same grain at step sizes of larger than around 250nm). Hence, the unannealed samples cannot be subjected to the thorough GND analysis, across various step size regimes, that is desired for the later discussion in this paper. Nevertheless, GND data at the smallest step size used in this study, 0.05 μm, can be used the compare the measured GND density after various

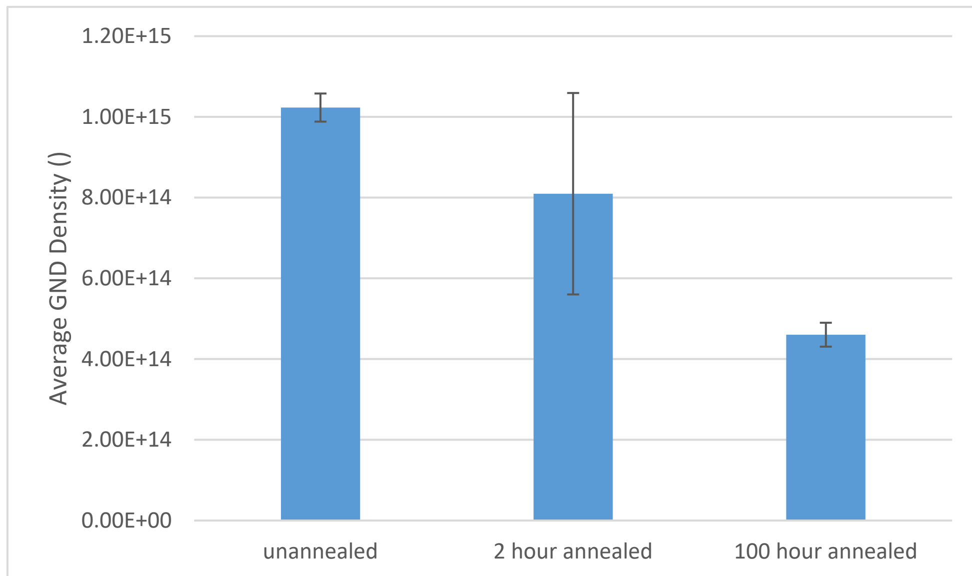

Figure 4-19: Graph of average GND measured in the wedge samples with a 0.05 μm step size.

annealing times. Data from the wedge specimens is used, as justified in the next section, and the meaningfulness of GND results collected as such a small step size is also discussed later. The results are presented in figure 4-3. The results generally agree with the prediction that GND density should go down with annealing time.

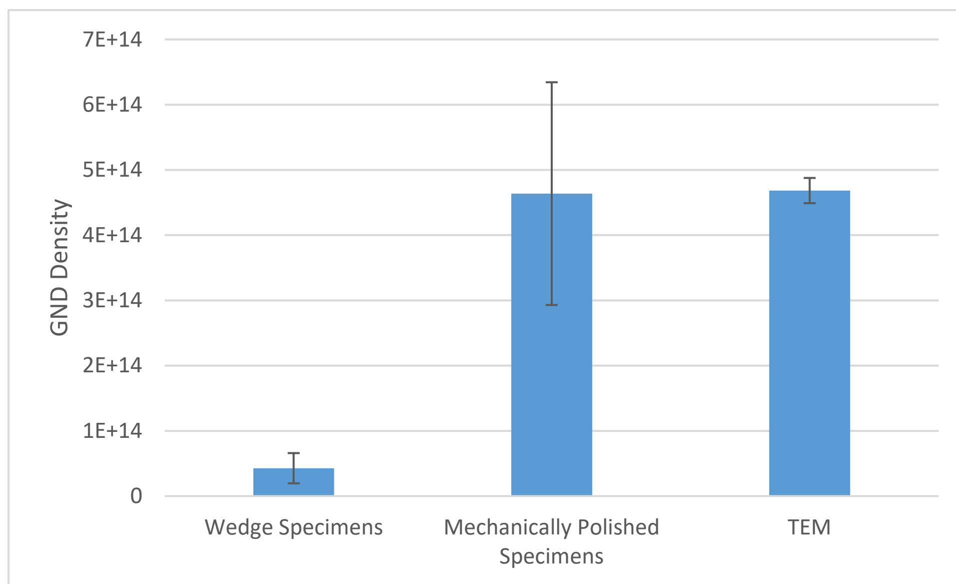

Figure 4-39: Graph of average HREBSD measured GND density at 1.2 µm step size for the platinum wire.

4.3 Effects of Specimen Geometry and Preparation on EBSD GND Measurements.

As can be seen in the graph in figure 4-4, the mechanically polished specimens showed a significantly higher dislocation density than the wedge specimens from the same wire, with an average value close to ten times higher. Figure 4-5 contains pole figures for mechanically polished and FIB-prepared wedge specimens of the same 70 µm wire. As can be seen, there is

substantial smearing across the pole figure of the mechanically polished specimen, indicating deformation of the relatively soft platinum (with a Vickers hardness of 40) during the polishing process, despite great care being taken. The local reorientation of the surface layer shows up as a higher GND content. Additionally, the pattern quality from the mechanically polished specimens was considerably poorer and despite the carbon coating the platinum specimens still suffered noticeably from charging.

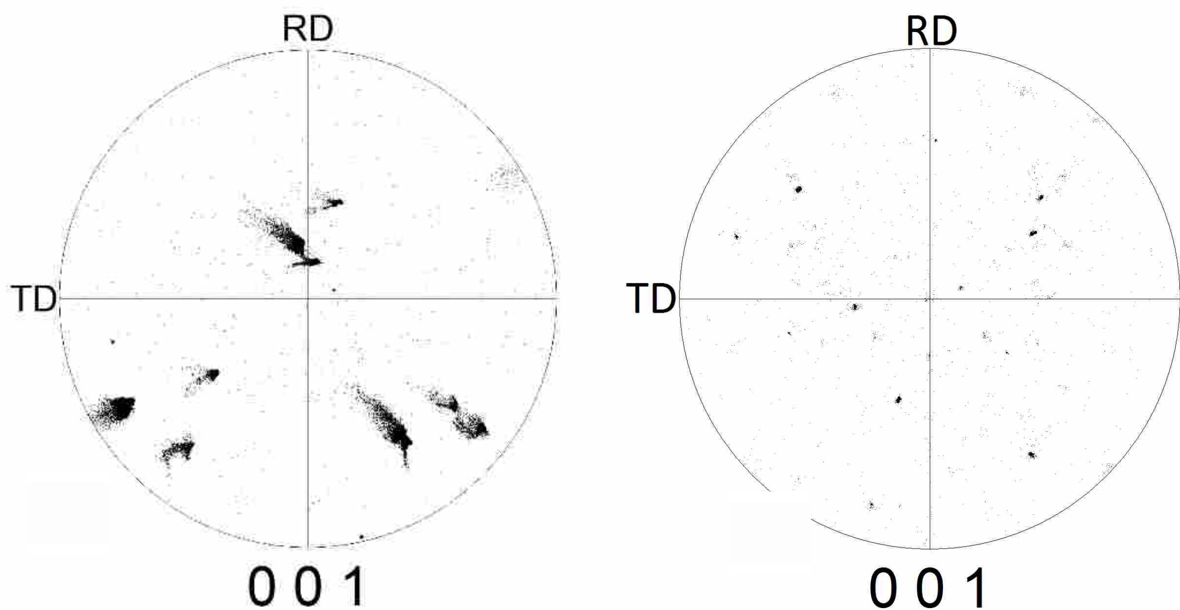

Figure 4-51: Inverse pole figure of a scans of the 70 µm 2 hours annealed specimens prepared with a) mechanical polishing and b) the FIB. Smearing of the grains is visible in the mechanically polished specimen pole figure.

These observations highlight that for certain samples, especially for soft metals and difficult geometries (such as the tiny wires, and resultant negative spaces around the wires which

can trap particulates), the generally used mechanical polishing techniques may be unreliable for preparing EBSD specimens for GND analysis.

Due to these low-quality patterns and the apparent damage to the material for the mechanically polished specimens, the fibbed wedge specimens were considered more reliable for assessing GND content than the mechanically polished ones.

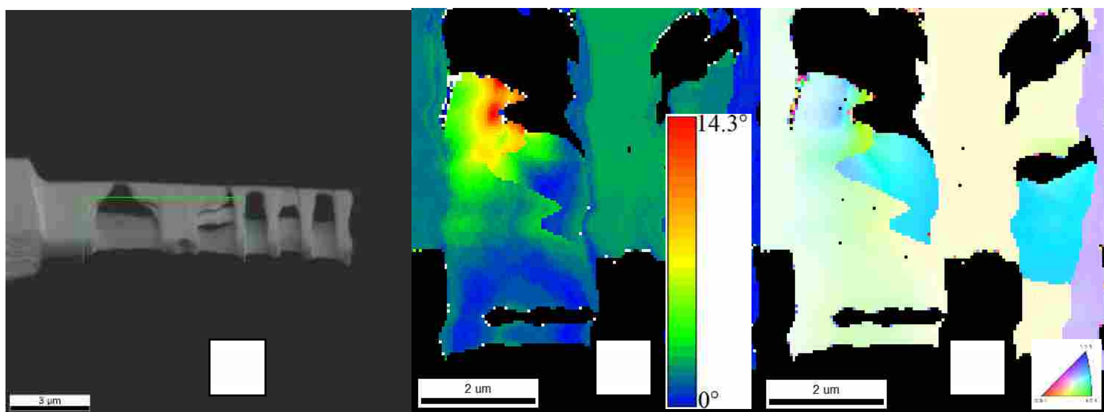

Figure 4-64: a) SEM image of a thin window removed from the 40 µm wire sample annealed for 100 hours, showing the scanned area, b) the grain reference orientation deviation map showing bending in the thin window, and c) The specimen IPF map.

Apart from the occultation issue mentioned above, the electron transparent thin window specimens were also observed to have warping along the window, likely from residual stresses. While not a problem for the TEM analsysis, HREBSD recorded this as an extraordinary amount of dislocations due to the bending in the crystal lattice. At a 1.2 µm step size, unthinned wedge specimens had an average measured GND density of $5.9 * 10^{13} \mu m^{-2}$.

Using a simplified version of Eq. 4, with only a single edge dislocation type, the GND density can be approximated by

$$\rho = \frac{\left[\frac{\sin^{-1}(d\theta)}{dx}\right]}{b} \tag{11}$$

where ρ is the dislocation density, $d\theta$ and dx are the misorientation and distance between measured points, and b is the Burgers vector, which for platinum is approximately $2.77 * 10^{-10} m$. Based upon the observed GND density, rotation from bending of just 0.9°/μm is enough to mask the actual GND. Figure 4-6 b shows the GROD (grain reference orientation deviation) map for a thin window specimen, illustrating that the bending can be of the order of 7 degrees per micron leading to large values of phantom GND density, up to ten times higher than measured in the wedge. Because of this we considered the EBSD GND measurements of the thin windows to be unreliable, and the EBSD from these specimens is not used in the future comparisons.

Issues with both the mechanically polished specimens and the FIBed thin windows mean that the most reliable GND results come from the FIBed wedge specimens. But these specimens were also prepared to try and determine whether thinning of the specimen near the wedge tip led to a change in dislocation density (e.g. due to dislocations escaping from the two free surfaces). Figure 4-7 provides several views of a wedge specimen, with the thin tip at the bottom of the images. The measured GND density from HREBSD remained relatively constant for most of the wedge, but near the tip there appeared to be a slight increase in dislocations, as opposed to the expected decrease (figure 4-7 b). Figure 4-7 c provides a GROD map, with consistent orientation values across the thicker part of the wedge, but with a significant warping on the tip (up to 10 degrees), similar to what was observed in the thin electron transparent windows.

Hence, the GND data in this region cannot be relied upon; i.e. these specimens cannot help determine whether dislocation density is modified by thinning samples to electron transparency.

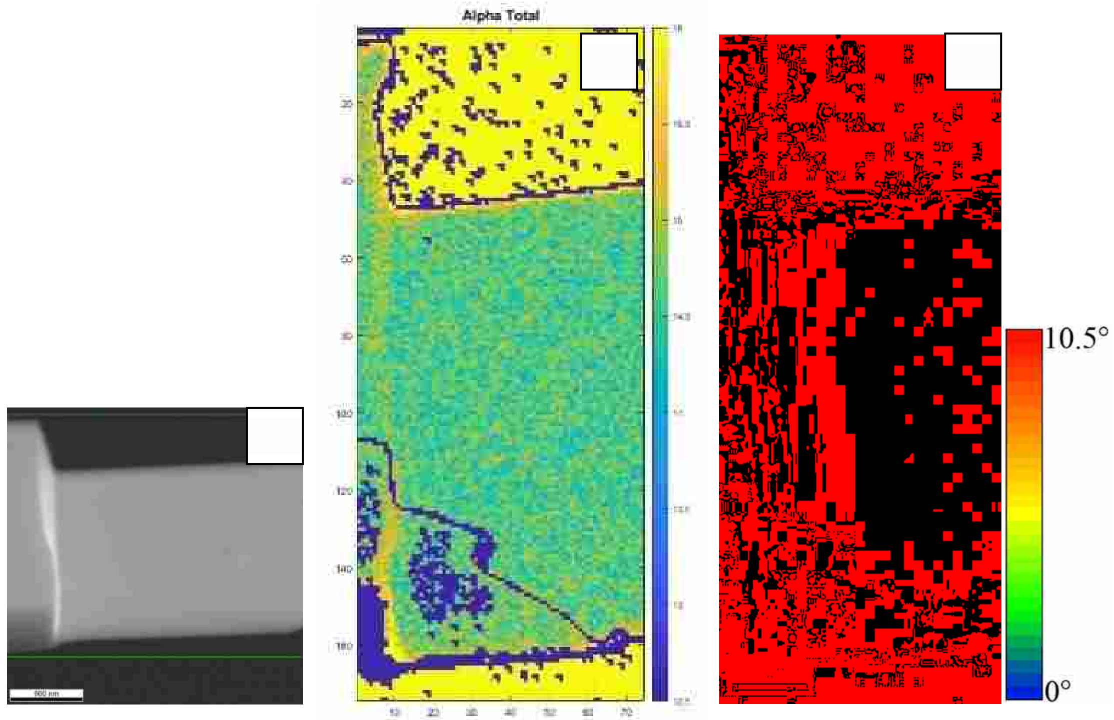

Figure 4-81: a) SEM Image, b) GND map and c) Grain Reference orientation map, showing the constant measured GND density across the majority of the wedge and increase and bending at the very tip (towards the bottom of the page.)

4.4 Comparison of HREBSD and TEM Results

As mentioned earlier, an indication of the likely change in dislocation content between the annealed samples can be gained from the change in resistance. Based on the resistance change reported by the temperature sensor manufacturer for the 40 µm wire of 512 micro ohm resistance drop for every 100 hours of extra annealing after the initial annealing period we would expect a total change in dislocation density of about $1.5 * 10^{12}/m^2$ from 2 to 100 hours of annealing by using equation 8 [22]. This is significantly smaller than the total dislocation

density measured in the TEM specimens, of approximately $4.8 * 10^{14}/m^2$, and is within the noise range of the TEM measurements, meaning we would not expect to see any significant trends between the different TEM specimens. This can be seen in figure 4-8, with a small decline in dislocation density apparent after 100 hours of annealing. The standard deviation of TEM measurements across all annealed samples is shown in figure 4-9.

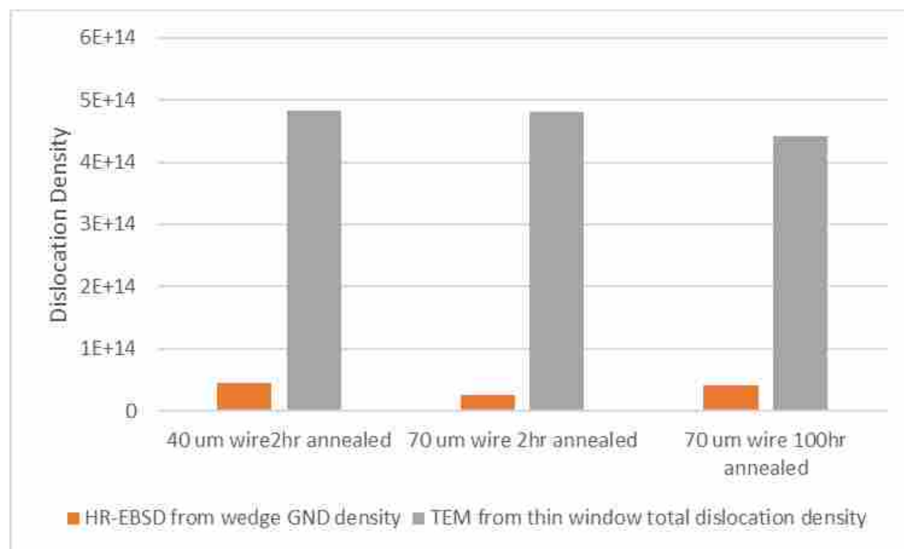

Figure 4-82: Graph of GND calculated from HREBSD at 1.2 µm step size and the total dislocation density measured in the TEM for different samples.

The HREBSD measurements were taken on the wedge specimens, prepared using the FIB and analyzed with a 1.2 µm simulated step size, as discussed earlier. The 1.2 µm step size was selected as being close to typically used values, while also being a multiple of the different step sizes used for the various scans of the wedges (0.05 µm, 0.15 µm, 0.2 µm); since EBSD patterns were saved from each of these step sizes for each specimen, distortions between points

1.2 μm apart could be determined for all three types of scan, as the basis for GND measurements. The resultant measured GND density values of $2.54 * 10^{13}/m^2$ to $4.53 * 10^{13}/m^2$ are between 10 and 20 times lower than the measured TEM values (see figures 4-8 and 4-9). For an annealed sample, having a low ratio of GND to total dislocation density may not be unreasonable. However, this points to the conclusion that at the usual step size (of around 1 μm) HREBSD is not an accurate tool for estimating total dislocation density on samples with such low ratios of GND-to-total dislocation content (e.g. for samples without significant plastic deformation).

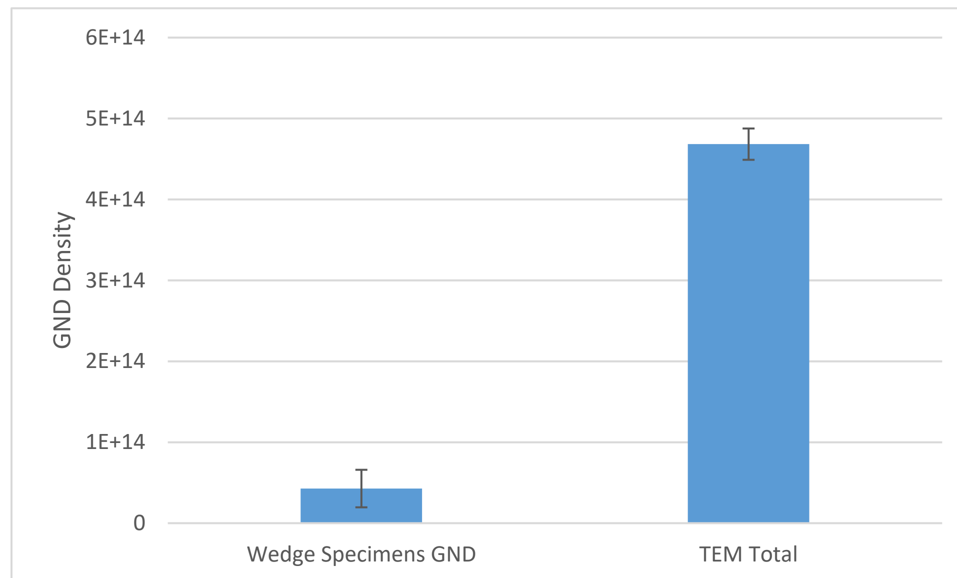

Figure 4-90: Graph of average GND calculated from HREBSD at 1.2 μm step size and the average total dislocation density measured in the TEM.

As noted, the 1.2 μm step size considered above is chosen to be close to the typical GND structure size. As the step size (and related virtual Burgers circuit) is reduced, more SSDs become GNDs; in the limit, every dislocation becomes a GND. Figure 4-10 illustrates the effect of step size on the measured GND content, compared with the single value of total dislocation content from TEM. It is interesting to note that when the step size was reduced to between 0.05

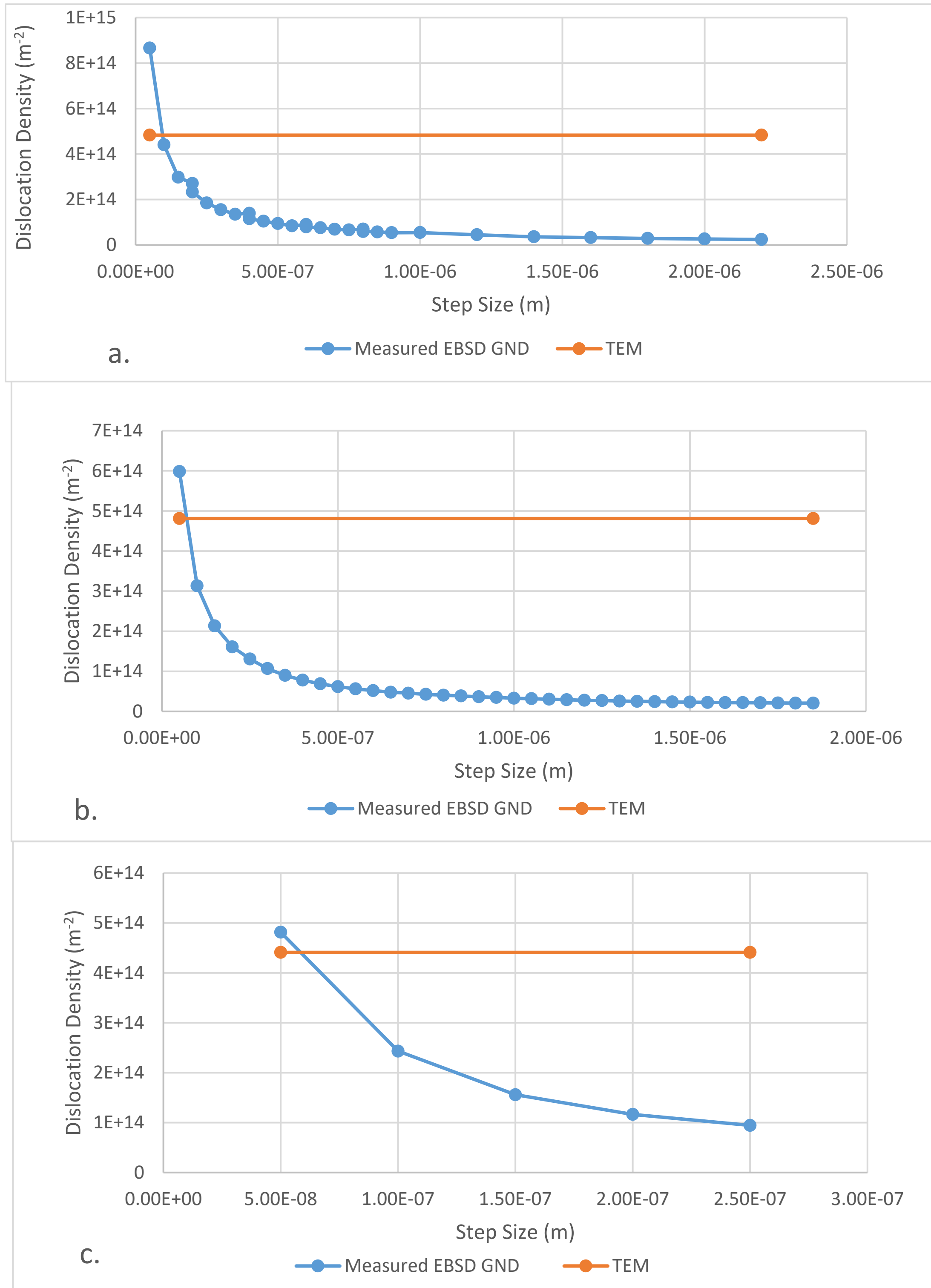

Figure 4-91: Graphs of step size vs calculated GND and the TEM measurements showing agreement between results between 0.05 and 0.1 µm, the approximate spacing for the dislocations as measured by the TEM for a) 40 µm 2hr annealed, b) 70 µm 2hr annealed, and c) 70 µm 100hr annealed platinum wire.

μm and 0.1 μm the measured GMD density was quite close to the dislocation density measured in the TEM. This step size is about the same as the average distance between dislocations at the dislocation density measured in the TEM (0.047 μm). While a rise in GND measurements can occur as step size is decreased simply due to noise, the slope of a curve resulting purely from a constant amplitude noise in the distortion measurement (Eq. 4) would follow 1/L (where L is the step size; see figure 4-11) [29]. Our scan in this range has a slope of $1/L^{0.85}$, indicating that this is not simply a result of noise, but relates to the actual SSD content becoming GND content. This suggests that as the step size approaches the average distance between dislocations, the

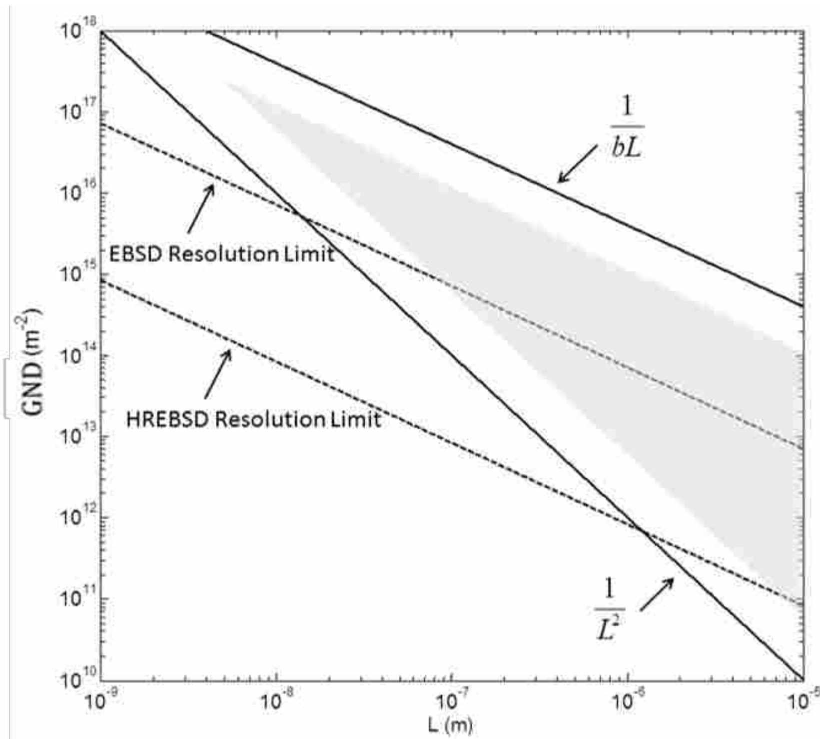

Figure 4-110: GND resolution vs step size from Kysar et al. The EBSD resolution assumes an orientation resolution of 0.5° and the HREBSD resolution limit assumes an orientation resolution of 0.006°. Both lines have a slope of 1/L.

statistically stored dislocations become GND's and the dislocation density measured using EBSD becomes a close match to that measure on the TEM. Unfortunately, this requires a priori knowledge of the dislocation content to provide the correct step size. It may be the case that the GND content vs step size curve transitions from a $1/L^k$ to a $1/L$ slope at this region of the curve, indicating the correct point where all SSDs had transitioned to GNDs; but smaller step sizes would be required than those used in this paper to traverse the desire region, and may be unreasonably small for standard EBSD.

4.5 Estimating Total Dislocation Density From EBSD Using Curve Fitting

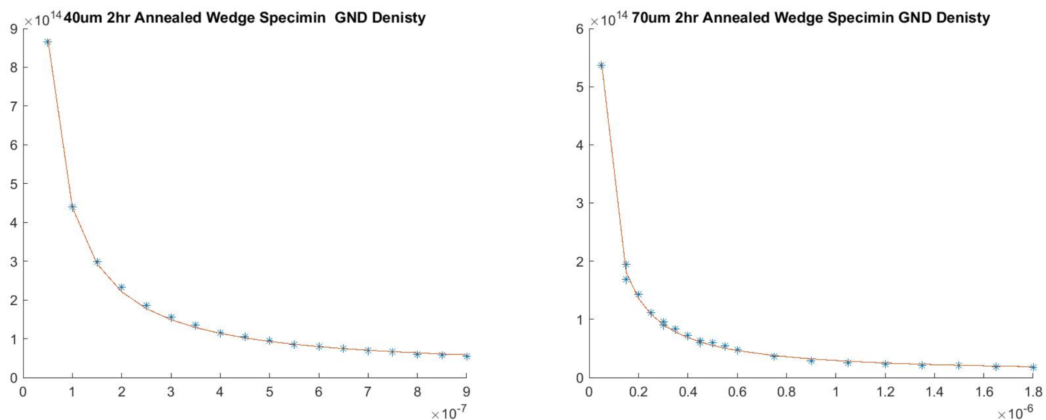

Figure 4-111: Calculated GND density at different step sizes vs the fit curve from Ruggles et al.'s GND vs step size equation for 40 µm and 70 µm 2 hr annealed wedge samples.

Another approach to estimating total GND content from HREBSD was suggested by Ruggles et al [5]. It was hypothesized that by fitting a curve to the graph of GND density vs step size, the total dislocation density, ρ_t, could be extracted from the curve parameters, ρ_t ρ_n and q

(Eq. 5). This approach was taken for the 40 µm and 70 µm wedge specimens, since these provided a good curve fit (over a large range of step sizes), and could be compared with TEM data (see figure 4-12 for the curve fits of two specimens). The values of total dislocation density from the Ruggles vs TEM approaches are shown in figure 4-13; the Ruggles values are between two and six time higher than the TEM measurements. It is possible that Ruggles equation overestimates the number of total dislocations due to a breakdown of the continuity assumption used in the HREBSD analysis, or that the measured step sizes did not represent a wide enough spread to accurately match all 3 parameters in the equation (due to the small specimens and grain sizes).

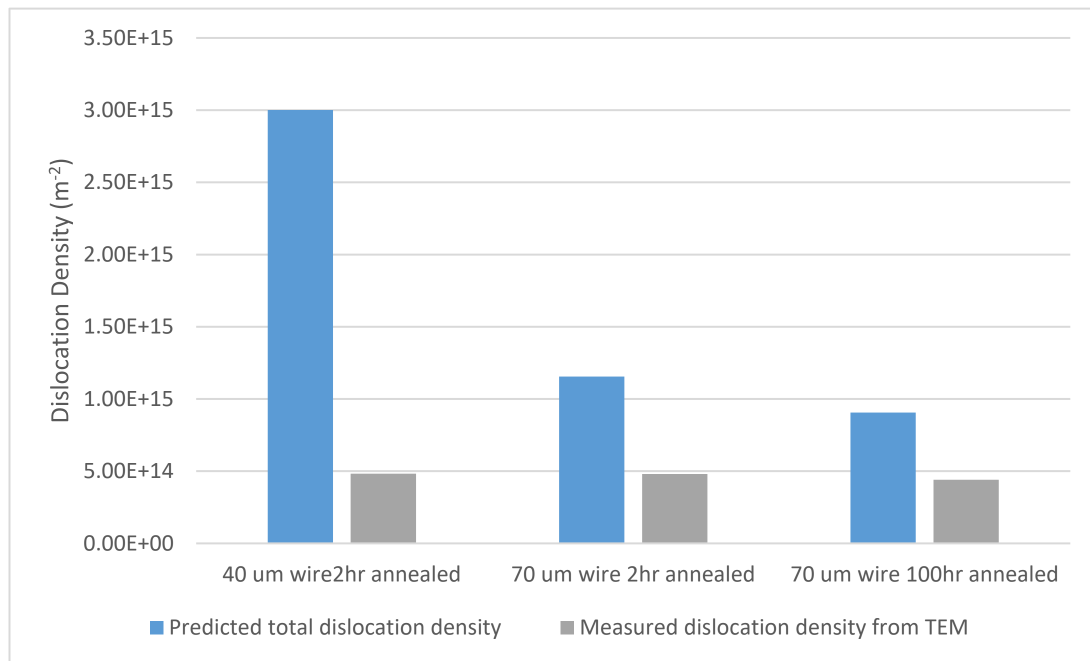

Figure 4-112: Predicted total dislocation density from Ruggles' equation vs the total dislocation density measured in the TEM.

5 CONCLUSION

The aim of this study was to determine the potential for using HREBSD to measure or estimate total dislocation content in a sample, and the impact of different sample preparation techniques and geometries on the HREBSD measurements. Mechanically polished and FIB lift-out specimens of two types (wedge and window) were prepared from 40 mm and 70 mm wire of Pt that were unannealed, or annealed to 2 or 100 hours.

The FIB liftout specimens presented an immediate issue, in that the geometry of the specimen and specimen holder were such that part of the electron yield was occulted by these components, leading to potential mis-indexing by the commercial EBSD software. However, the shadowed regions did not extend into the areas of the EBSD patterns used for GND analysis. A simple confidence index filter was used to remove points where misindexing might occur.

It was found that mechanical polishing of the soft Pt wires resulted in significant smearing of the lattice orientation on the polished surface, resulting in apparent GND densities of over ten times higher than the specimens prepared using FIB. The FIB specimens did not suffer from the smearing issue.

Thin window specimens prepared by the FIB liftout method developed high amounts of curvature across the windows, resulting in high calculations of GND content by the analysis software due to the large orientation gradients. This made direct comparison of dislocation content by the HREBSD and TEM methods on the same specimen unattainable. Other sample

preparation techniques (reviewed in the background section) might also be able to produce a larger thin area with less bending, to determine what effect thinning has on the dislocation density.

Hence dislocation data was taken from the liftout wedge specimens for HREBSD and from the thin window specimens for TEM. The wedge specimens were shaped so as to be able to determine whether dislocation density was reduced as the specimen became extremely thin (potentially due to dislocations escaping to the free surfaces), but bending in the region of the wedge tip did not allow this analysis, for the same reasons mentioned for the thin windows.

The grain size of the sample also influenced the ability to use HREBSD to determine its GND density at reasonable step sizes. The sub-micron grains of the unannealed specimens did not allow GND analysis at typical step sizes of 1-2 μm. While there did appear to be a trend towards lower dislocation density with annealing time, as expected, when observed at 0.05 μm step size, analysis at larger step sizes was not possible.

At the typically used step size of 1-2 μm the wedge liftout specimens showed very low GND density compared to the total dislocation density measured by the TEM. For an annealed sample, having a low ratio of GND-to-total dislocation density may not be unreasonable. However, this points to the conclusion that for such materials, and at a typical step size (of around 1 μm), HREBSD is not an accurate tool for estimating total dislocation density. HREBSD based dislocation measurements are likely to be more effective on samples that have a large degree of plastic deformation resulting in the GND's making up a high percentage of the total dislocation density.

One of the most interesting results of this study was the agreement of the GND measured using HREBSD on the wedge specimens and the total dislocation density measured on the TEM when the EBSD step size was equal to the average spacing between dislocations. To check that the HREBSD data was not dominated by noise at this step size, the slope of the log-log graph of GND vs step size was examined. A curve create purely by noise should have a slope of 1/L, so the observed slope of ~ $1/L^{0.85}$ (typical of GND curves in the known regions of low noise) indicates that the graph is dominated by the actual dislocation density. Since the total dislocation density would not be known in a practical situation, and hence the correct step size selected, it may be possible to observe the slope of the graph and note where it transforms into a 1/L relation to provide an approximate step size for determining total dislocation density. Unfortunately, the 0.05 µm step size used for the finest step size in this study was too large to observe this transition, and the lack of significant change in dislocation density between the useable samples in this study made it impossible to test this relation at other dislocation densities.

Ruggles et al.'s method for estimating total dislocation density, by fitting an assumed curve of measured GND vs step size, was inaccurate at determining the total dislocation density (being 2 to 6 times higher than the measured TEM values). The maximum step size available from the EBSD data was fairly small, potentially affecting the results. Larger grained samples would allow for a greater spread of step sizes, making relations between the step size, the GND density, and the total dislocation density, including Ruggles et al.'s equation easier to test.

It is also possible that this formula has other inaccuracies since Nye Kroner is a continuum theory and at this very small step size it starts to break down, as the SEM is starting to observe individual dislocations.

Additional studies using samples with greater variations in dislocation density, especially densities that can be predicted based on deformation could provide more conclusive evidence of the capabilities of EBSD to estimate dislocation density. This would allow for the GND density vs total dislocation density to be observed and compared at multiple values to get a better idea of their relation.

REFERENCES

1. Gardner, C.J., et al., *EBSD-based continuum dislocation microscopy.* International Journal of Plasticity, 2010. **26**: p. 1234-1247.

2. Wilkinson, A.J. and D. Randman, *Determination of elastic strain fields and geometrically necessary dislocation distributions near nanoindents using electron back scatter diffraction.* Philosophical Magazine, 2010. **90**(9): p. 1159-1177.

3. Williams, D.B. and C.B. Carter, *Transmission Electron Microscopy*. 1996, New York: Springer Science.

4. Schwartz, A.J., et al., eds. *Electron backscatter diffraction in materials science 2nd Ed.* Second ed. 2009, Springer: New York.

5. Ruggles, T.J., et al., *The effect of length scale on the determination of geometrically necessary dislocations via EBSD continuum dislocation microscopy.* Ultramicroscopy, 2016. **164**: p. 1-10.

6. Jiang, J., T.B. Britton, and A.J. Wilkinson, *Measurement of geometrically necessary dislocation density with high resolution electron backscatter diffraction: Effects of detector binning and step size.* Ultramicroscopy, 2013. **125**: p. 1-9.

7. Prins, J.F. and H.G.F. Wilsdorf, *DISLOCATION INTERACTIONS IN THE IMMEDIATE VICINITY OF A FREE SURFACE.* Canadian Journal of Physics, 1967. **45**(2): p. 1177-1187.

8. G Webster, J. and H. Eren, *Measurement, Instrumentation, and Sensors Handbook: Spatial, Mechanical, Thermal, and Radiation Measurement*. 2014.

9. Hull, D. and D.J. Bacon, *Introduction to Dislocations*. fifth ed. 2011, The Boulevard, Langford Lane, Kidlington, Oxford, OX5 1GB: Elsevier Ltd. 257.

10. Hirsch, P.B., ed. *Topics in Electron Diffraction and Microscopy of Materials*. 1999, Institute of Physics Publishing.

11. Ham, R.K., *The determination of dislocation densities in thin film.* Philosophical Magazine, 1961. **6**: p. 1181-1184.

12. Wright, S.I. and M.M. Nowell, *EBSD Image Quality Mapping.* Microscopy and Microanalysis, 2006. **12**: p. 72-84.

13. Wright, S., M. Nowell, and J. Basinger, *Precision of EBSD based orientaion measurements.* Microscopy & Microanalysis, 2011. **17**: p. 406-407.

14. Fullwood, D., et al., *Microstructure Detail Extraction via EBSD: An Overview*, in *Strains and dislocation gradients from diffraction*, R. Barrabas and G.E. Ice, Editors. 2014, Imperial College Press.

15. Nye, J.F., *Some geometrical relations in dislocation solids.* Acta Metallurgica, 1953. **1**(2): p. 153--162.

16. Pantleon, W., *Resolving the goemetrically necessary dislocation content by conventional electron backscattering diffraction.* Scripta Materialia, 2008. **58**: p. 994-997.

17. Ruggles, T. and D. Fullwood, *Estimations of Bulk Geometrically Necessary Dislocation Density Using High Resolution EBSD.* Ultramicroscopy, 2013. **133**: p. 8-15.

18. Wilkinson, A.J., G. Meaden, and D.J. Dingley, *High-resolution elastic strain measurement from electron backscatter diffraction patterns: New levels of sensitivity.* Ultramicroscopy, 2006. **106**: p. 307-313.

19. Preston-Thomas, H., *The International Temperature Scale of 1990 (ITS-90).* Metrologia, 1990. **27**(1): p. 3-10.

20. H Meyers, C., *Coiled Filament Resistance Thermometers*. Vol. 9. 1932.

21. Kocer, M., et al., *Measurement of Dislocation Density by Residual Electrical Resistivity.* Materials Science Forum, 1996. **210-213**: p. 133-140.

22. Watts, B.R., *Conduction electron scattering in dislocated metals*. Vol. 8. 1989. 175-419.

23. Mayer, J., et al., *EM Sample Preparation and FIB-Induced Damage.* MRS Bulletin, 2007. **32**: p. 400-407.

24. Giannuzzi, L. and F. Stevie, *Introduction to Focused Ion Beams*. 2004.

25. Mayer, J., et al., *TEM Sample Preparation and FIB-Induced Damage.* MRS Bulletin, 2007. **32**(5): p. 400-407.

26. Bethe, H.A., *Theory of Atomic Collisions.* Nature, 1951. **167**(4240): p. 165-165.

27. Ahn, C.C., et al., *EELS atlas : a reference collection of electron energy loss spectra covering all stable elements*. 1983, Tempe, Ariz.; Warrendale, PA: HREM Facility, Center for Solid State Science, Arizona State University ; Gatan, Inc.

28. BYU, *OpenXY*. 2015, github.com.

29. Kysar, J.W., et al., *Experimental lower bounds on geometrically necessary dislocation density.* International Journal of Plasticity, 2010. **26**: p. 1097-1123.